



# Nature of Faint Radio Sources in GOODS-North and GOODS-South Fields. I. Spectral Index and Radio–FIR Correlation

Hansung B. Gim<sup>1,2</sup> , Min S. Yun<sup>2</sup> , Frazer N. Owen<sup>3</sup> , Emmanuel Momjian<sup>3</sup> , Neal A. Miller<sup>4</sup>, Mauro Giavalisco<sup>2</sup> , Grant Wilson<sup>2</sup> , James D. Lowenthal<sup>5</sup> , Itziar Aretxaga<sup>6</sup> , David H. Hughes<sup>6</sup>, Glenn E. Morrison<sup>7,8</sup> , and Ryohei Kawabe<sup>9,10,11</sup> 

<sup>1</sup> School of Earth and Space Exploration, Arizona State University, Tempe, AZ 85281, USA; [Hansung.Gim@asu.edu](mailto:Hansung.Gim@asu.edu)

<sup>2</sup> Department of Astronomy, University of Massachusetts, Amherst, MA 01003, USA

<sup>3</sup> National Radio Astronomy Observatory, P.O. Box O, Socorro, NM 87801, USA

<sup>4</sup> Department of Mathematics and Physical Sciences, Stevenson University, 1525 Greenspring Valley Road, Stevenson, MD 21153, USA

<sup>5</sup> Department of Astronomy, Smith College, Northampton, MA 01063, USA

<sup>6</sup> Instituto Nacional de Astrofísica, Óptica y Electrónica, Luis Enrique Erro 1, Sta. Ma. Tonantzintla, 72000, Puebla, Mexico

<sup>7</sup> LBT Observatory, University of Arizona, 933 N. Cherry Avenue, Room 552, Tucson, AZ 85721, USA

<sup>8</sup> Canada–France–Hawaii Telescope, Kamuela, Hawaii, HI 96743, USA

<sup>9</sup> National Astronomy Observatory of Japan, Osawa, Mitaka, Tokyo, 181-8588, Japan

<sup>10</sup> The Graduate University for Advanced Studies (SOKENDAI), 2-21-1 Osawa, Mitaka, Tokyo 181-0015, Japan

<sup>11</sup> Department of Astronomy, School of Science, University of Tokyo, Bunkyo, Tokyo 113-0033, Japan

Received 2018 October 23; revised 2019 March 6; accepted 2019 March 13; published 2019 April 17

## Abstract

We present the first results from the deep and wide 5 GHz radio observations of the Great Observatories Origins Deep Survey (GOODS)-North ( $\sigma = 3.5 \mu\text{Jy beam}^{-1}$ , synthesized beam size  $\theta = 1''.47 \times 1''.42$ , and 52 sources over 109 arcmin<sup>2</sup>) and GOODS-South ( $\sigma = 3.0 \mu\text{Jy beam}^{-1}$ ,  $\theta = 0''.98 \times 0''.45$ , and 88 sources over 190 arcmin<sup>2</sup>) fields using the Karl G. Jansky Very Large Array. We derive radio spectral indices  $\alpha$  between 1.4 and 5 GHz using the beam-matched images and show that the overall spectral index distribution is broad even when the measured noise and flux bias are considered. We also find a clustering of faint radio sources around  $\alpha = 0.8$ , but only within  $S_{5 \text{ GHz}} < 150 \mu\text{Jy}$ . We demonstrate that the correct radio spectral index is important for deriving accurate rest-frame radio power and analyzing the radio–FIR correlation, and adopting a single value of  $\alpha = 0.8$  leads to a significant scatter and a strong bias in the analysis of the radio–FIR correlation, resulting from the broad and asymmetric spectral index distribution. When characterized by specific star formation rates, the starburst population (58%) dominates the 5 GHz radio source population, and the quiescent galaxy population (30%) follows a distinct trend in spectral index distribution and the radio–FIR correlation. Lastly, we offer suggestions on sensitivity and angular resolution for future ultra-deep surveys designed to trace the cosmic history of star formation and AGN activity using radio continuum as a probe.

*Key words:* galaxies: active – galaxies: starburst – galaxies: star formation – radio continuum: general – surveys

## 1. Introduction

Stellar mass buildup and central massive black hole growth are two key observational constraints for understanding galaxy evolution in modern astronomy. A significant fraction of these activities are heavily obscured by dust over the cosmic history (Le Floch et al. 2005; Caputi et al. 2007; Magnelli et al. 2011; Whitaker et al. 2017), and we need another tracer that can penetrate deep into column densities exceeding  $N_{\text{H I}} > 10^{24} \text{ cm}^{-2}$  ( $A_V \gg 100$ ). The completion of the NSF’s Karl G. Jansky Very Large Array<sup>12</sup> (VLA) with a more than 100 times larger spectral bandwidth and a new powerful digital correlator translates to more than an order of magnitude improvement in sensitivity to probe star formation and black hole activities at cosmological distances (Perley et al. 2011).

The low-frequency ( $\nu \lesssim 10 \text{ GHz}$ ) radio sky is dominated by synchrotron emission (Condon 1992), which mainly comes from star-forming galaxies (SFGs) and active galactic nuclei (AGNs). In SFGs, synchrotron emission is generated through cooling of cosmic rays accelerated by shocks associated with SNe II. In AGN, synchrotron radiation is produced by relativistic charged

particles in radio cores and jets. Different origins of the observed synchrotron radiation are encoded in radio spectral index  $\alpha$ , which is defined as  $S \propto \nu^{-\alpha}$ , where  $S$  is the flux density and  $\nu$  is the frequency. Star-forming regions are optically thin to synchrotron radiation, which yields a steep, characteristic radio spectral index of  $\alpha \approx 0.8$  (Condon 1992). Synchrotron emission in AGN is produced in two different ways. Radio core AGN are optically thick enough to absorb synchrotron emission and re-emit, which makes the slope of the synchrotron radiation flatter (“synchrotron self-absorption”),  $\alpha \ll 0.8$  (de Bruyn 1976). In jets, relativistic electrons lose their energy over time while traveling down the length of the jets and the resulting radio spectral index is steeper (“synchrotron aging”),  $\alpha > 0.8$  (e.g., Burch 1979).

Radio spectral indices have been used to study the nature of radio sources. In particular, the emergence of flat spectrum sources in the sub-mJy regime has been reported by several authors (e.g., Donnelly et al. 1987; Prandoni et al. 2006; Randall et al. 2012), although others have reported no flattening in the mean spectral index (Fomalont et al. 1991; Ibar et al. 2009). Deeper radio observations with  $\mu\text{Jy}$  sensitivity have shown that the fraction of steep spectrum sources increases with decreasing flux density, suggesting the emergence of SFGs at the sub-mJy level (Ibar et al. 2009; Huynh et al. 2015; Murphy et al. 2017), in agreement with the interpretation of the normalized number

<sup>12</sup> The National Radio Astronomy Observatory is a facility of the National Science Foundation operated under cooperative agreement by Associated Universities, Inc.

**Table 1**  
Observation Summary

Field	R.A. (J2000)	Decl. (J2000)	Date	Duration
GN	12 <sup>h</sup> 36 <sup>m</sup> 31 <sup>s</sup> .3	62°10′50″.0	2011 Feb 28	5.5 hr
			2011 Mar 10	5.5 hr
	12 <sup>h</sup> 37 <sup>m</sup> 07 <sup>s</sup> .5	62°14′51″.0	2011 Mar 15	5.5 hr
			2011 Mar 20	5.5 hr
GS	03 <sup>h</sup> 32 <sup>m</sup> 30 <sup>s</sup> .00	−27°43′45″.0	2012 Dec 16	2.5 hr
	03 <sup>h</sup> 32 <sup>m</sup> 13 <sup>s</sup> .33	−27°45′52″.5	2012 Dec 23	2.5 hr
	03 <sup>h</sup> 32 <sup>m</sup> 13 <sup>s</sup> .33	−27°50′07″.5	2012 Dec 31	2.5 hr
	03 <sup>h</sup> 32 <sup>m</sup> 30 <sup>s</sup> .00	−27°52′15″.0	2013 Jan 1	2.5 hr
	03 <sup>h</sup> 32 <sup>m</sup> 46 <sup>s</sup> .67	−27°50′07″.5	2013 Jan 5 (1)	2.5 hr
	03 <sup>h</sup> 32 <sup>m</sup> 46 <sup>s</sup> .67	−27°45′52″.5	2013 Jan 5 (2)	2.5 hr

counts (Owen & Morrison 2008; Condon et al. 2012) and the analysis of the polarization (Rudnick & Owen 2014). A radio study of submillimeter galaxies has showed that their radio spectral index distribution is a skewed Gaussian with a peak near  $\alpha \sim 0.7$  and a tail toward flatter spectrum (Ibar et al. 2010). These studies indicate a promising potential for the radio spectral index as a tracer of underlying physical activity in distant galaxies.

We show here that obtaining *correct* measurements of radio spectral indices is critically important in calculating the rest-frame radio power and for understanding the cosmic evolution of the faint radio population. Any uncertainty in radio spectral index translates directly to the uncertainty in derived radio power, and this in turn affects the accuracy of the radio-far-infrared (FIR) correlation analysis (Gim et al. 2015; Delhaize et al. 2017). Radio AGNs with jets are often resolved by interferometric observations, and even normal SFGs show spatially resolved structures at arcsecond scales (e.g., Chapman et al. 2004; Barger et al. 2017).

In this paper, we present the analysis of radio spectral indices between 1.4 and 5 GHz derived with matched beams, for a large sample of faint radio sources identified from the deep and wide 5 GHz radio observations on the Great Observatories Origins Deep Survey (GOODS)-North (GN) and GOODS-South (GS) fields. We examine the correlations among radio spectral index, radio-FIR correlation, and star formation properties. We also discuss the limitations of radio observations tracing normal SFGs, the importance of correct derivation of radio spectral index, and the constraints provided by radio spectral index to classifying radio SFGs. Throughout this paper we adopt the cosmological parameters,  $H_0 = 67.8 \text{ km s}^{-1} \text{ Mpc}^{-1}$ ,  $\Omega_m = 0.308$ , and  $\Omega_\Lambda = 0.692$  (Tanabashi et al. 2018).

## 2. Observations

### 2.1. Radio Observations

#### 2.1.1. GOODS-North

Our observations of the GN field were conducted in 2011 February and March, for a total of 22 hr at 5 GHz in the B-configuration of the VLA under the program code 10C-225. As summarized in Table 1, we observed two fields with the VLA’s Wideband Interferometric Digital Architecture (WIDAR) correlator, which was configured to deliver two 128 MHz sub-bands in full polarization. The sub-bands were further split into  $64 \times 2$  MHz channels each, and centered at 4896 and 5024 MHz, respectively. The correlator integration time was 3 s.

The calibration and reduction of the VLA data were carried out using the standard data reduction package Astronomical Image Processing System (AIPS). The flux calibrator 3C286 was used for the calibrations of delay, flux density scale, and polarization, while the gain calibrator J1400+6210 was used for the bandpass and gain calibration. The radio quasar J1400+6210 is bright enough (1.72 Jy at 5 GHz) to be used for the bandpass calibration.

Imaging of the visibility data was performed using the Common Astronomy Software Applications (CASA; McMullin et al. 2007). The wide-field imaging of each field was carried out using nine facets, each with  $4096 \times 4096$  pixels with a cell size of  $0''.35$ , down to  $3\sigma$ . The Clark point-spread function (PSF) model is adopted, and the Briggs function is used to weight the data with a robust value of  $R = 1$ . The Briggs weighting function is intermediate between natural (lowest noise, poorest resolution) and uniform (highest noise, best resolution) weighting functions, and the robust factor of  $R = 1$  gives an optimal compromise between sensitivity and resolution. The final mosaic and sensitivity images incorporating the primary-beam correction are produced using the AIPS tasks LTESS and STESS, respectively. The final mosaic image has a size of  $5120 \times 5120$  pixels, centered at  $[12^{\text{h}}36^{\text{m}}49^{\text{s}}.4, 62^{\circ}12'50''.5]$  (J2000), with a synthesized beam of  $1''.47 \times 1''.42$ . The effective central frequency of the image is 4.959 GHz (hereafter 5 GHz) with a total bandwidth of 240 MHz. The final noise is  $\sigma = 3.5 \mu\text{Jy beam}^{-1}$  in the image center. The survey coverage map for the GN field is shown in panel (A) of Figure 1.

#### 2.1.2. GOODS-South

The GS field was observed at 5 GHz for a total of 15 hr in the A-configuration of the VLA under the project code of 12B-274. The coordinates of the six pointing centers and observation dates are listed in Table 1. The WIDAR correlator was configured to deliver sixteen 128 MHz sub-bands, each with  $64 \times 2$  MHz channels and full polarization products. The frequency span was from 4488 to 6512 MHz. Correlator integration time was 1 s to minimize the time smearing effect. The observations were executed in six different sessions, each with 2.5 hr long.

Data reduction and imaging were performed using CASA. The flux density scale calibrator 3C48 was used for the calibrations of delay, flux scale, and polarization, while the gain calibrator J0240−2309 (2.33 Jy at 5 GHz) was used for calibrations of bandpass, phase, and delay. Severe radio-frequency interference (RFI) dominated the last four SPWs (12–15), and they are excluded in the analysis. Self-calibration was carried out successfully to improve the overall dynamic range of the image using bright sources ( $>1 \text{ mJy}$ ) in each field.

Initial imaging was done in CASA for each field and each SPW exploiting the wide-field imaging with 36 facets that are each  $10,240 \times 10,240$  pixels in size and using a cell size of  $0''.1$ , down to  $3\sigma$ . The Clark PSF and the Briggs weighting function with a robust value of  $R = 0.8$  are adopted for imaging. The synthesized beam depends on the frequency, and all images are convolved to match the largest beam at the lowest frequency SPW before the final mosaic image is constructed. Using the weights of  $w_i = (\text{beam area})_{\text{new}} / (\text{beam area})_{\text{old}}$ , all images were convolved to have beam sizes of  $0''.98 \times 0''.45$ . The mosaic image of each SPW is produced first using the AIPS tasks LTESS and STESS with primary-beam correction. The final band-merged image is

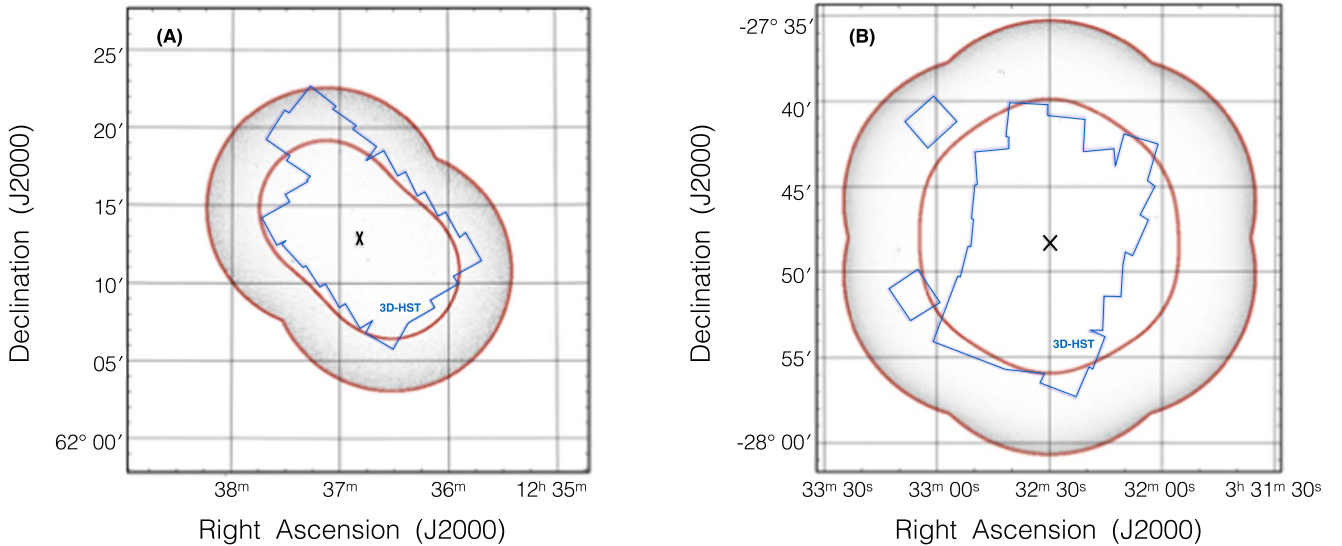


**Figure 1.** VLA 5 GHz mosaic images for the GN (panel (A)) and the GS (panel (B)) fields. The inner red contours trace the boundary where the primary-beam correction increases the effective noise to twice that in the image center, and this also marks the survey area where the source catalogs are derived. The outer red contours mark the survey areas where the primary-beam response is 7% of the mosaic center. The centers of each mosaic are marked with a cross (“x”), and the 3D-HST coverages are outlined in blue polygons.

produced by averaging the SPW mosaic images using the  $1/\sigma^2$  weight, where  $\sigma$  is an rms noise of each mosaic. The final band-merged mosaic image is  $16384 \times 16384$  pixels in size with the central frequency of 5.245 GHz (hereafter 5 GHz) and a total bandwidth of 1.486 GHz. The rms noise in the center of the mosaic is  $\sigma = 3.0 \mu\text{Jy beam}^{-1}$ , and the coverage map centered on  $[03^{\text{h}}32^{\text{m}}30^{\text{s}}0, -27^{\circ}48'00'']$  is shown in panel (B) of Figure 1.

### 2.1.3. Source Catalogs

The 5 GHz sources are extracted from primary-beam corrected images using the AIPS task SAD. Since RFI is time-dependent and the primary-beam response is not uniform, the final noise distribution is not uniform or symmetric across the mosaic. Therefore, we limit the source search for generating the catalogs to the central regions with up to twice the rms noise in primary-beam corrected maps (i.e.,  $7 \mu\text{Jy beam}^{-1}$  for the GN field and  $6 \mu\text{Jy beam}^{-1}$  for the GS fields as shown with inner red contours in Figure 1). We also minimized the impact of the effective frequency shift to lower frequency toward the edge of the final image. Since the coverage of the image is different at each SPW due to the frequency-dependent primary-beam correction, the effective frequency moves to the lower frequency toward the edge of the frequency-stacked image. We have created a matching sensitivity map to track the frequency-dependent effects in the final mosaic. We also limited our catalog to the more central region reasonably far away from the edges. Sources detected with a peak signal-to-noise ratio (S/N)  $> 5$  are selected for the final catalogs, and the measured flux densities are corrected for bandwidth smearing by setting the AIPS adverb BWSMEAR as the fraction of channel width with respect to the central frequency in the SAD. However, the time averaging effect is not taken into account since its impact on the flux density is small enough ( $< 0.1\%$ ) to be neglected within our catalog regions (Bridle & Schwab 1999). The final catalogs include 52 and 88 sources in the GN and GS fields covering 109

and 190 arcmin<sup>2</sup> areas, respectively. These catalogs are shown in Appendix B.

### 2.1.4. Comparisons with Previous Results

There are recent radio continuum observations of both GN and GS fields with comparable or higher sensitivity and at a higher angular resolution, and they offer an interesting and complementary view on the nature of the faint radio source population. Guidetti et al. (2017) have studied the GN field at 5.5 GHz with an rms noise of  $3 \mu\text{Jy beam}^{-1}$  and a synthesized beam size of  $0''.5$ , and they reported a total of 94 sources ( $\geq 5\sigma$ ) over their  $154 \text{ arcmin}^2$  survey area. This is about a 80% larger number of sources over a 50% larger area with a similar flux density sensitivity compared to our survey. At least part of this difference must be due to their three times smaller beam (nine times worse surface brightness sensitivity), which can fragment some of the resolved SFGs and jet sources into multiple components. Guidetti et al. (2017) also suggested this surface brightness sensitivity effect as the root cause for their unexpectedly large (80%) AGN fraction.

Earlier surveys of the GS field by Kellermann et al. (2008) at 4.9 GHz using the VLA and by Huynh et al. (2015) 5.5 GHz using the Australia Telescope Compact Array were both about a factor of two shallower in sensitivity ( $\sigma \approx 8 \mu\text{Jy}$ ) and two to three times lower in angular resolution ( $\theta \approx 4''$ ) compared to our survey. Huynh et al. (2015) reported finding 212 source components over their  $0.34 \text{ deg}^2$  survey area down to a flux density of  $\sim 50 \mu\text{Jy}$  ( $\geq 5\sigma$ ). Kellermann et al. (2008) did not report the source count in their 4.9 GHz VLA survey, but Huynh et al. (2015) reported their data to be consistent because of their similar resolution and sensitivity. The 5 GHz source density derived from these surveys with  $\sim 3$  times shallower depth is 2.6 times lower than our survey.

More recently, Rujopakarn et al. (2016) have observed the Hubble Ultra Deep Field (HUDF) within the GOODS-South at 6 GHz with an rms noise of  $0.32 \mu\text{Jy beam}^{-1}$  at an angular resolution of  $0''.61 \times 0''.31$ . A direct comparison of the source density is difficult in this case because these authors report two

source counts that are not fully reflective of the true source density: (1) a total of 68 “bright” ( $\geq 8\sigma$ ) sources within the 61 arcmin<sup>2</sup> survey region extending beyond the primary beam; and (2) a total of 11 sources detected at  $\geq 5\sigma$  among the 13 sources detected by ALMA inside the 40.7 arcmin<sup>2</sup> ALMA survey area. The former number offers a more useful comparison, and corresponds to about 2.5 times higher source density at 6–8 times better sensitivity compared with our survey. The latter number is strictly a lower limit, since it includes only ALMA-detected sources at  $z = 1-3$ . The resulting source density is only 60% of the source density we derive, despite their 10 times better flux density sensitivity.

In summary, the source density we derive is consistent with those of the past surveys. A striking trend seen is that the derived source density increases relatively slowly with improved sensitivity. There are potentially important systematic differences in how the catalogs are generated, and these source counts are not corrected for completeness in a consistent way. Nevertheless, the rise in source density with improving depth of the survey is far flatter than the Euclidean case. Along with the improving sensitivity, subsequent observations have also employed higher angular resolution, and this might play an important role in the derived source statistics, as discussed further in Section 7.2. This also serves as one of our motivations for using beam-matched data for our spectral index analysis (see Section 4).

## 2.2. Multiwavelength Data

### 2.2.1. VLA 1.4 GHz

1.4 GHz data are needed to calculate the radio spectral index with our 5 GHz data. For the GN field, we use the deep 1.525 GHz (hereafter 1.5 GHz) imaging data obtained by Owen (2018) with rms noise of  $2.2 \mu\text{Jy beam}^{-1}$  and an angular resolution of  $1''.6 \times 1''.6$  (FWHM). Owen (2018) have used different beam sizes ( $2''$ ,  $3''$ ,  $6''$ , and  $12''$ ) to measure the flux densities of extended sources because those sources were resolved out with the original beam size, which resulted in the prevention of the loss of flux densities. All of our 5 GHz sources have a matching counterpart in the 1.5 GHz source catalog.

For the GS field, we use the 1.4 GHz VLA data by Miller et al. (2013), which has rms noise of  $\sim 6 \mu\text{Jy beam}^{-1}$  at the image center with a beam size of  $2''.8 \times 1''.6$ . Since the beam area of these 1.4 GHz data is about 10 times larger than our 5 GHz data and the depth of the 1.4 GHz data is significantly shallower than in the GN field, matching the counterparts to the 5 GHz sources is more complicated. We convolve the 5 GHz images for each field and SPW to yield a beam size of  $2''.8 \times 1''.6$  using the AIPS task CONVL, and the final mosaic is produced by summing over all pointings and SPW using the AIPS tasks LTESS and STESS.<sup>13</sup> The rms noise of the convolved 5 GHz image is slightly higher,  $6.4 \mu\text{Jy beam}^{-1}$ . We generated the  $3\sigma$  catalog from the convolved image using

the AIPS task SAD. For the 38 sources that were not found in this  $3\sigma$  catalog due to increased noise and low completeness at low S/N, we manually performed aperture photometry on the convolved image centered on the source coordinates from the original, full resolution image. A total of 83 sources are identified in the final convolved 5 GHz mosaic image with a beam size of  $2''.8 \times 1''.6$ , as eight of the sources in the original catalog are now blended into three sources. Matching the 1.4 GHz catalog with this beam-matched 5 GHz data yields 64 counterparts among the 83 sources. A total of 19 sources lack a 1.4 GHz counterpart because the 1.4 GHz data are too shallow ( $5\sigma \geq 30 \mu\text{Jy beam}^{-1}$  at the image center) to detect 5 GHz sources with a flat or inverted spectrum which is a characteristic of some of the radio AGNs (see panels (D) and (E) of Figure 4). Throughout this paper, we analyze only the GS sources that have a unique 1.4 GHz counterpart to avoid the uncertainty introduced by the upper limits.

### 2.2.2. Chandra X-Ray Observatory

We use X-ray data taken from the *Chandra X-Ray Observatory* survey with full band (0.5–7 keV), soft band (0.5–2 keV), and hard band (2–7 keV) catalogs. We make use of 2 Ms observations for the GN field (Xue et al. 2016) and 7 Ms observations for the GS field (Luo et al. 2017). The limiting fluxes for the GN field are  $3.5 \times 10^{-17}$ ,  $1.2 \times 10^{-17}$ ,  $5.9 \times 10^{-17} \text{ erg cm}^{-2} \text{ s}^{-1}$  at full band, soft band, and hard band, respectively. For the GS field, the limiting fluxes are  $1.9 \times 10^{-17}$  at full band,  $6.4 \times 10^{-18}$  at soft band, and  $2.7 \times 10^{-17} \text{ erg cm}^{-2} \text{ s}^{-1}$  at hard band. To calculate the X-ray luminosity, we assume a photon index of  $\Gamma = 1.8$  for X-ray detected radio sources (Tozzi et al. 2006) but  $\Gamma = 1.4$  for X-ray undetected radio sources (Luo et al. 2017). The full band X-ray luminosity at [0.5–7 keV] is converted to the luminosity at [0.5–8 keV] using the relation of  $L_{[0.5-8 \text{ keV}]} = 1.066 \times L_{[0.5-7 \text{ keV}]}$  for the assumed  $\Gamma = 1.8$  (Xue et al. 2016).

### 2.2.3. Spitzer Space Telescope

We exploit publicly released *Spitzer Space Telescope* (*Spitzer*) IRAC catalogs of the GN (Wang et al. 2010) and GS (Damen et al. 2011) fields. The GN field IRAC catalog has a sensitivity ( $1\sigma$ ) of  $0.15 \mu\text{Jy}$  at  $3.6 \mu\text{m}$ , while the GS field IRAC catalog by the *Spitzer* IRAC/MUSYC Public Legacy Survey in the Extended *Chandra* Deep Field-South (ECDFS) has a sensitivity ( $1\sigma$ ) of  $0.22 \mu\text{Jy}$  at  $3.6 \mu\text{m}$ . We make use of the high angular resolutions of our radio observations to find counterparts within the beam sizes (i.e.,  $1''.47$  for the GN and  $0''.98$  for the GS fields).

### 2.2.4. Herschel Space Observatory

The comparison FIR data are constructed using the public archival data for the Photodetector Array Camera and Spectrometer (PACS) and the Spectral and Photometric Imaging Receiver (SPIRE) of the *Herschel Space Observatory*.<sup>14</sup> The PACS photometry data at 70, 100, and 160  $\mu\text{m}$  are taken from the combination of PACS Evolutionary Probe (Lutz et al. 2011, PEP) and GOODS-*Herschel* (Elbaz et al. 2011) programs described by Magnelli et al. (2013). The SPIRE 250, 350, and 500  $\mu\text{m}$  photometry data are taken from the *Herschel*

<sup>13</sup> Since the final radio image is a combination of cleaned components with flux density scaled by clean beam and residuals with flux densities weighted by dirty beam, the convolution of the radio image with the clean beam includes the convolution of the residuals scaled by the dirty beam, in addition to the convolution of the clean components scaled by the clean beam. The former contributes to the uncertainty of the convolved images, but it is not easy to estimate its contributions because it involves many parameters, such as clean thresholds, PSF shape, and the convolution kernel size. This is a subtle but notable systematic effect that we have decided to ignore for the moment.

<sup>14</sup> *Herschel* is an ESA space observatory with science instruments provided by European-led Principal Investigator consortia and with important participation from NASA.

Multi-tiered Extragalactic Survey (HerMES) DR 3 and 4 (Roseboom et al. 2010, 2012; Magnelli et al. 2011). We adopt the catalogs extracted using the *Spitzer* MIPS 24  $\mu\text{m}$  position priors for the PACS bands by the GOODS-*Herschel* collaboration.<sup>15</sup> As for the SPIRE bands, we used the catalogs extracted at the SPIRE 250  $\mu\text{m}$  source positions (HerMES DR4).<sup>16</sup>

To identify FIR counterparts to the radio sources, we apply the likelihood ratio technique (Sutherland & Saunders 1992). The search radius adopted is three times the combined positional uncertainties of the radio and *Herschel* sources. Sources with the reliability of  $\text{Rel}_i > 0.8$ <sup>17</sup> are accepted as formal counterparts. We consider an FIR source to be the counterpart to a radio source if it is detected in at least one band in both PACS and SPIRE, with a S/N > 4 in at least one band.

We have compiled the observed 24, 100, 160, 250, 350, and 500  $\mu\text{m}$  band fluxes of 40 GN and 44 GS sources. The best-fit FIR SED models are identified using a widely used SED fitting code Le Phare<sup>18</sup> (Arnouts et al. 1999; Ilbert et al. 2006) with various SED templates for SFGs (Chary & Elbaz 2001; Dale et al. 2001; Lagache et al. 2003) and QSOs (Polletta et al. 2007). This analysis yielded a good SED model for 39 GN and 42 GS sources. For the radio sources undetected at FIR or with a poor-fit SED, we calculate IR luminosity with  $4\sigma$  flux limits adopting the average  $z = 1$  SFG SED template (Kirkpatrick et al. 2012).

### 2.2.5. Spectroscopic Redshifts

Spectroscopic redshifts are compiled from the published surveys: GN (Cowie et al. 2004; Donley et al. 2007; Barger et al. 2008; Wirth et al. 2015) and GS (Szokoly et al. 2004; Zheng et al. 2004; Mignoli et al. 2005; Ravikumar et al. 2007; Vanzella et al. 2008; Popesso et al. 2009; Straughn et al. 2009; Balestra et al. 2010; Silverman et al. 2010; Cooper et al. 2012; Kurk et al. 2013; Le Fèvre et al. 2013; Skelton et al. 2014; Morris et al. 2015), respectively. From these compilations, we have 45 (out of 52) sources with spectroscopic redshifts for the GN and 55 (out of 64) for the GS field. In particular, all 55 GS sources with a spectroscopic redshift are in the subsample of 64 sources with both 1.4 and 5 GHz photometry used for the spectral index analysis.

Even though reliable photometric redshifts from well-sampled photometry data exist in both fields, we limit our analysis to only those with a spectroscopic redshift because errors in redshift translate directly to a large scatter and systematic biases in the derived quantities such as the rest-frame radio power, radio–FIR correlation, and star formation rate (SFR). A detailed evaluation of the accuracy of the existing photometric redshifts and a quantitative analysis on the magnitude of error introduced by using photometric redshifts using this spectroscopic subsample are presented in Appendix A. Adding those sources with only photometric redshifts to our statistical analysis can in principle expand our sample by up to 16%, but we have elected to remove this major source of scatter in our statistical analyses presented here for now.

<sup>15</sup> Data are available at <http://www.mpe.mpg.de/ir/Research/PEP/DR1>.

<sup>16</sup> Data are available at <http://hedam.lam.fr/HerMES/index/dr4>.

<sup>17</sup> Reliability is defined as  $\text{Rel}_i = \text{LR}_i / (\sum \text{LR}_i + (1 - q_0))$  for the likelihood ratio  $\text{LR}_i$  and the fraction of true counterparts above the detection limit,  $q_0$ .

<sup>18</sup> Le Phare is available at <http://www.cfht.hawaii.edu/~arnouts/lephare.html>.

### 2.2.6. 3D-HST

We adopt physical parameters such as stellar mass, SFR, and effective radius for our 5 GHz sources that also appear in the 3D-*HST*<sup>19</sup> (Brammer et al. 2012; Skelton et al. 2014; Momcheva et al. 2016) database. Stellar mass is estimated by the FAST code (Kriek et al. 2009) with the Chabrier (2003) initial mass function, and the Bruzual & Charlot (2003) stellar population synthesis library (Skelton et al. 2014). The SFR is computed through the conversion of UV+IR luminosity, where UV luminosity is derived from the rest-frame luminosity at 2800 Å, and IR [8–1000  $\mu\text{m}$ ] luminosity is derived from *Spitzer* MIPS 24  $\mu\text{m}$  flux density by assuming the log average of Dale & Helou (2002) templates (see Whitaker et al. 2014). Effective radius ( $R_{\text{eff}}$ ) is the semimajor axis of the ellipse containing one half of the total flux of the best Sérsic model given by GALFIT (van der Wel et al. 2012).

The spectroscopic redshifts given in the 3D-*HST* database are not as complete as our compilation, and we have to match our spectroscopic redshifts with the best redshifts in the 3D-*HST* database, which ranks them by spectroscopic, grism, or photometric redshift. A comparison of the best 3D-*HST* redshifts with our spectroscopic redshifts is shown in Figure 2. We choose the 3D-*HST* counterparts with best redshifts satisfying  $|z_{\text{spec}} - z_{\text{best,3D-HST}}| / (1 + z_{\text{spec}}) < 0.05$ , which is shown with dashed lines in Figure 2. Spectroscopic redshifts of the best redshifts in 3D-*HST* are mostly the same as ours, while there are some small to significant offsets in grism and photometric redshifts. Through matching the redshifts, we have 3D-*HST* counterparts for 39 GN and 45 GS radio sources.

## 3. Selection Function and Rest-frame 5 GHz Radio Power

In Figure 3, we show the selection function of our radio sources with rest-frame 5 GHz radio power as a function of redshift. The rest-frame radio power is calculated using the measured spectral index as

$$P_{5 \text{ GHz}} = 4\pi d_L^2 S_{5 \text{ GHz}} (1 + z)^{\alpha-1} [\text{W Hz}^{-1}], \quad (1)$$

where  $d_L$  is the luminosity distance,  $S_{5 \text{ GHz}}$  is the measured 5 GHz flux density of the original map, and  $\alpha$  is the measured radio spectral index between 1.4 and 5 GHz using the convolved map (see Section 4). The strong positive  $k$ -correction associated with radio sources translates to a significant selection bias in favor of flat spectrum sources ( $\alpha = 0$ , dashed line) with lower intrinsic radio power, but such flat spectrum sources are rare in our sample, as shown in this plot (also see Figure 4). The selection functions of the two fields are similar with comparable mean and median values of 5 GHz radio power and redshifts, and a joint analysis of the combined sample is reasonable as long as the slight difference in the catalog depth is properly taken into account.

The majority of the detected sources have rest-frame 5 GHz radio power between  $10^{22}$  and  $10^{24}$   $\text{W Hz}^{-1}$ , which is the range of radio power associated with intense starburst systems (LIRGs, ULIRGs) and Seyfert nuclei in the local universe. However, gas content and SFR of star-forming main-sequence

<sup>19</sup> This work is based on observations taken by the 3D-*HST* Treasury Program (GO 12177 and 12328) with the NASA/ESA *HST*, which is operated by the Association of Universities for Research in Astronomy, Inc., under NASA contract NAS5-26555.

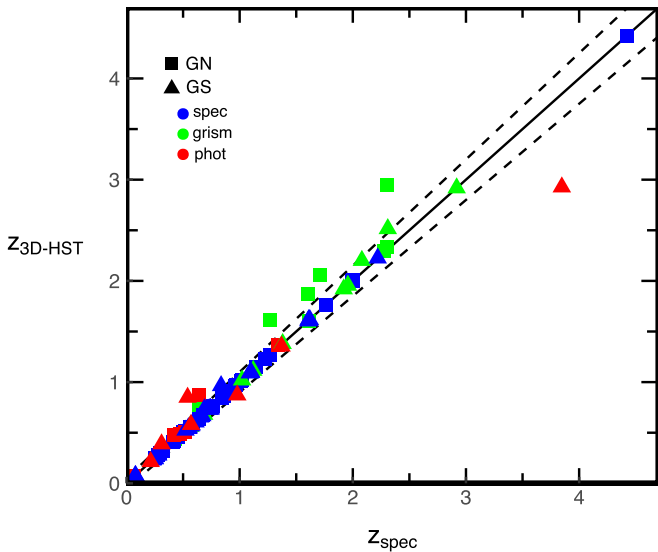


**Figure 2.** Comparison of our spectroscopic redshifts and the best redshifts in 3D-*HST* for the GN (square) and the GS (triangle) fields. The color represents the type of redshift measurements—for example, spectroscopy (blue), grism (green), and photometry (red). The solid line is the one-to-one line and dashed lines show the selection limits of  $|z_{\text{spec}} - z_{\text{best,3D-HST}}| / (1 + z_{\text{spec}}) < 0.05$ .

(MS) galaxies are known to increase rapidly with increasing redshift by an order of magnitude to  $z \geq 1$  (e.g., Speagle et al. 2014; Scoville et al. 2017), and a large fraction of these galaxies at higher redshifts are likely powered by star formation, discussed as follows. Only four sources (two in each field) have a radio power high enough to be classified as “radio-loud” with  $P_{5 \text{ GHz}} \geq 10^{25} \text{ W Hz}^{-1}$  (Miller et al. 1990).

#### 4. Radio Spectral Index

Radio spectral index  $\alpha$  is a measure of the shape of a radio spectrum characterized as a power-law,  $S \sim \nu^{-\alpha}$ . We compute the spectral index between 1.4 and 5 GHz using the flux densities derived from the 5 GHz images beam-matched to the 1.4 GHz images, as described in Section 2.2.1. In principle, the radio spectral index can be estimated using only the 5 GHz data with its wide bandwidth of 1.5 GHz through the multifrequency synthesis. The algorithm that can produce in-band spectral index calculation for mosaic observations was not available in CASA when the data were being analyzed. The significant changes in the size of both the primary beam and the synthesized beam across the bandwidth make this in-band spectral index calculation challenging, especially away from the pointing center. These difficulties result in the errors of the in-band spectral index that are not competitive with those using the full 1.4–5 GHz spectral baseline. It is empirically shown that the majority of radio sources in a wide range of redshifts show radio spectra that are fit well with a simple power law (e.g., Klammer et al. 2006). In the frequency range between 1.4 and 5 GHz, the contribution by free-free emission is generally negligibly small (Condon 1992).

The distributions of radio spectral index as a function of flux density are shown in Figure 4. Panels (A), (B), and (C) are for the GN field while panels (D), (E), and (F) are for the GS field. Since the sensitivity for radio spectral index (dotted line) depends on the flux density limit of the second band (dashed lines), it is not uniform as a function of flux density, and this is

a common but important feature for all flux-limited surveys. Specifically, this non-uniform completeness limits our study to a narrower range of radio spectral indices at fainter flux densities. For our 5 GHz selected sample analyzed here, the depth of the existing 1.4 GHz data restricts the observable range of radio spectral index. We can see this effect clearly in panel (D), where the range of the radio spectral indices is limited to  $\alpha > 0$  even at  $S_{5 \text{ GHz}} = 30 \mu\text{Jy}$  ( $10\sigma$ ), and this can potentially lead to missing sources with inverted spectra at flux densities of  $S_{5 \text{ GHz}} < 30 \mu\text{Jy}$ . In practice, however, few inverted spectrum sources with  $S_{5 \text{ GHz}} < 35 \mu\text{Jy}$  ( $10\sigma$ ) are found in the GN field (panel (A)), and the actual impact of this potential bias may be limited.

The uncertainties in the derived radio spectral indices are mainly attributed to the larger uncertainties of flux densities at 5 GHz for the GN field and flux densities at 1.4 GHz for the GS field. The radio spectral index distribution in the GS field is broader and smoother than that in the GN field, and this can be attributed to the shallow depth of the 1.4 GHz data and the noisier 5 GHz photometry as a result of the convolution with a larger Gaussian kernel. Another source of the uncertainty is the wide bandwidth of the VLA. The effective frequency of each flux density measurement depends on the bandwidth and the spectral shape of the source, and this could lead to a significant offset of the effective frequency from the instrumental frequency. For the steepest spectrum source with  $\alpha = 1.64$  in the GS field, we estimate that this effect can lead to a maximum frequency offset of 0.1 GHz and a maximum deviation of 0.02 in the derived radio spectral index. Thus, we conclude that this effect has only a minor impact on our radio spectral index calculation. When these systematic effects are taken into account, the distributions of radio spectral indices in these two fields are consistent with each other.

Panel (A) in Figure 4 shows a clustering of radio sources at  $\alpha \sim 0.75$  and  $S_{5 \text{ GHz}} \leq 150 \mu\text{Jy}$ , leading to a prominent peak in the histogram in panel (C). The peak of the radio spectral index histogram for the GS field (panel (F)) occurs at the same  $\alpha$  value, but the clustering is not as pronounced, possibly diluted and broadened by the larger uncertainties in the measured radio spectral indices (see panels (B) and (E)). This peak in the  $\alpha$  of steep spectrum radio sources at  $S_{5 \text{ GHz}} \leq 150 \mu\text{Jy}$  has not been reported by earlier studies (e.g., Donnelly et al. 1987; Fomalont et al. 1991), but their small sample size (30 in Donnelly et al. 1987 and 41 in Fomalont et al. 1991) likely contributed to their poor statistics. A more recent study of a larger sample by Huynh et al. (2015), who measured radio spectral indices of 5.5 GHz selected sources above  $S_{5.5 \text{ GHz}} \gtrsim 50 \mu\text{Jy}$  in the ECDFS using the 1.4 GHz catalog of Miller et al. (2013), did report a spectral index distribution with a clear peak near  $\alpha \sim 0.7$ , as long expected of the SFG population (see the discussion that follows). We note that Huynh et al. (2015) computed their radio spectral index without matching the beam sizes (about a factor of 2.2 in diameter), and this might be a source of an important systematic error—see further discussions in Section 7.3.

A natural explanation for the peak near  $\alpha \sim 0.7$  is the contribution by the SFG population. Synchrotron emission is optically thin when it is produced by the shocks associated with supernovae in SFGs (Condon 1992; Seymour et al. 2008). The flattening or upturn in the number counts of radio sources

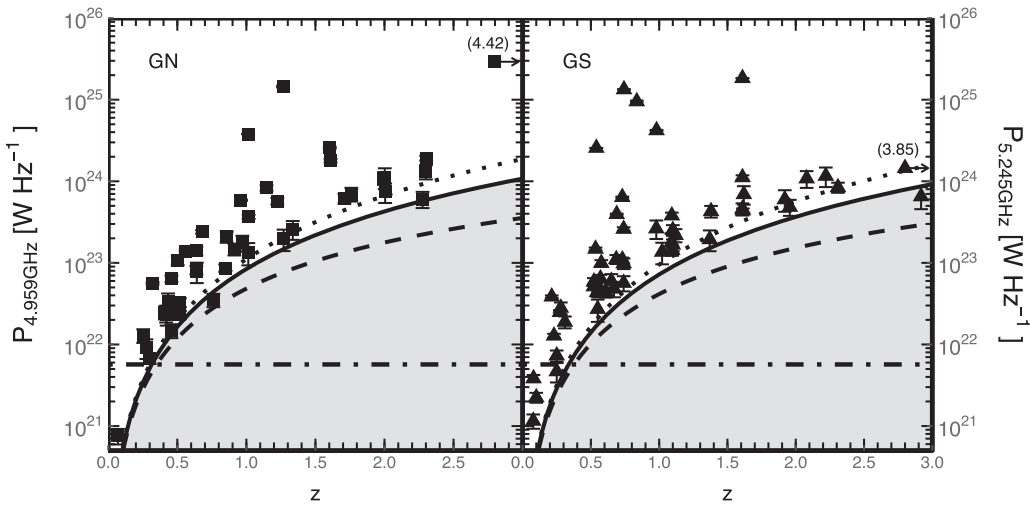


**Figure 3.** Rest-frame 5 GHz radio power as a function of redshift. Only the radio sources with a spectroscopic redshift are shown. The  $5\sigma$  detection limits are shown for radio spectral index of  $\alpha = 0$  (dashed line), 0.8 (solid line), and 1.2 (dotted line), where  $S \propto \nu^{-\alpha}$ . The horizontal dotted-dashed line at  $P_{5\text{ GHz}} = 5.7 \times 10^{21} \text{ W Hz}^{-1}$  corresponds to a luminous infrared galaxy (LIRG) with a SFR =  $10 M_{\odot} \text{ yr}^{-1}$ . Sources with redshift beyond 3 are marked with arrows, and their redshifts are written inside the parentheses.

seen around  $S_{20\text{ cm}} \leq 100\text{--}200 \mu\text{Jy}$  (Owen & Morrison 2008; Condon et al. 2012) is explained by the emergence of this population of SFGs at faint flux density levels, exceeding those of the radio-loud AGN population that is dominant at flux densities  $\geq 1 \text{ mJy}$ . The increase of fractional polarization and the change of slope in the polarized number count at polarized flux densities  $\leq 1 \text{ mJy}$  also imply the increasing contribution of SFGs (Rudnick & Owen 2014). The broad radio spectral index distributions for the GS and GN fields shown in Figure 4 suggests the existence of both steep spectrum ( $\alpha = 0.5\text{--}1.0$ ) and flatter or inverted spectrum ( $\alpha < 0.5$ ) sources at  $S_{5\text{ GHz}} < 150 \mu\text{Jy}$ , supporting the conclusions of the more recent analyses indicating that the faint  $\mu\text{Jy}$  radio population consist of both SFGs and radio-quiet AGN (Padovani et al. 2009; Bonzini et al. 2013; Rudnick & Owen 2014). A detailed study of a small sample of 14 local SFGs by Klein et al. (2018) has shown that there is also some scatter in the observed radio spectral index in the GHz range due to a varying degree of free-free emission and opacity effects. What our study further indicates is that a larger sample with higher quality radio spectral index measurements are needed to characterize the relative contribution by these two populations.

## 5. Star Formation Properties of Radio Sources

In the previous section, we have shown and discussed the distributions of radio spectral indices derived between 1.4 and 5 GHz from the beam-matched images. In this section, we investigate how the radio spectral index correlates with star formation properties by utilizing the SFRs and stellar masses derived by the 3D-*HST* project (Skelton et al. 2014; Momcheva et al. 2016).

### 5.1. $\Delta_{\text{SFR}}$ as a Measure of SF Activity

The distributions of SFR and stellar mass of radio sources in GN (squares) and GS (triangles) are shown in four redshift bins in Figure 5. The dashed lines indicate the SFR-stellar mass relation of the star-forming MS at a mean redshift in each panel, and the shaded regions represent dispersions of SFR-stellar mass relation at the MS with  $\log_{10} \text{SFR} - \log_{10} \text{SFR}(\text{MS}) = \pm 0.2$  (Speagle et al. 2014). As Speagle et al. (2014) and others noted,

the MS evolves strongly with redshift, and it is not clear whether the SFRs measured at different redshifts can be compared directly in a meaningful way. A more insightful measure might be the level of SF activity normalized by that of the MS at the same redshift. Therefore, we define “ $\Delta_{\text{SFR}}$ ,” the logarithm of the ratio of SFR with respect to that of the MS, as

$$\Delta_{\text{SFR}} \equiv \log_{10} \text{SFR} - \log_{10} \text{SFR}(\text{MS}), \quad (2)$$

where SFR(MS) is the SFR for the star-forming MS galaxy at a given stellar mass and redshift calculated using Equation (28) by Speagle et al. (2014).

Following Speagle et al. (2014), we define “SFGs” as galaxies with  $-0.2 \leq \Delta_{\text{SFR}} \leq 0.2$ , “starbursts (SBs)” as those with  $\Delta_{\text{SFR}} > 0.2$ , and “quiescent galaxies” as those with  $\Delta_{\text{SFR}} < -0.2$ . In total, we have 49 SBs (58%), 10 SFGs (12%), and 25 quiescent galaxies (30%). The dominance of the SB population among the  $\mu\text{Jy}$  radio population identified by one of the deepest surveys thus far is somewhat surprising, but this reflects the selection bias driven by the survey depth as discussed further below (also see Section 7.1).

In Figure 6, we show the distribution of  $\Delta_{\text{SFR}}$  as a function of stellar mass, color-coded by radio spectral index,  $\alpha$ . Quiescent galaxies detected in radio continuum are on average more massive than the SFG+SB while the SFG+SB show a wider range of stellar masses as shown in Figure 6. The median stellar masses are  $3.8 \times 10^{10} M_{\odot}$  for SFG+SB and  $9.3 \times 10^{10} M_{\odot}$  for quiescent galaxies, respectively. The two-sided Kolmogorov-Smirnov test for two samples in R (R Core Team 2017) indicates that stellar mass distributions in both populations are substantially different with a  $p$ -value of  $< 4.3 \times 10^{-5}$ . This significant difference in mass distributions is consistent with the mass quenching scenario for quiescent galaxies (e.g., Kauffmann et al. 2003).

The majority of our radio sources (58%) show intense star formation activity with  $\Delta_{\text{SFR}} > 0.2$ , while only 12% of radio sources fall within the range of MS SFGs with  $-0.2 < \Delta_{\text{SFR}} < 0.2$ . For comparison, we show the 3D-*HST* galaxies without radio counterparts (light gray) in Figure 6. In the same stellar mass range as the radio sources ( $\log M_{*} \geq 9.08$ ), the 3D-*HST* galaxies undetected in radio are classified into SBs (25%),

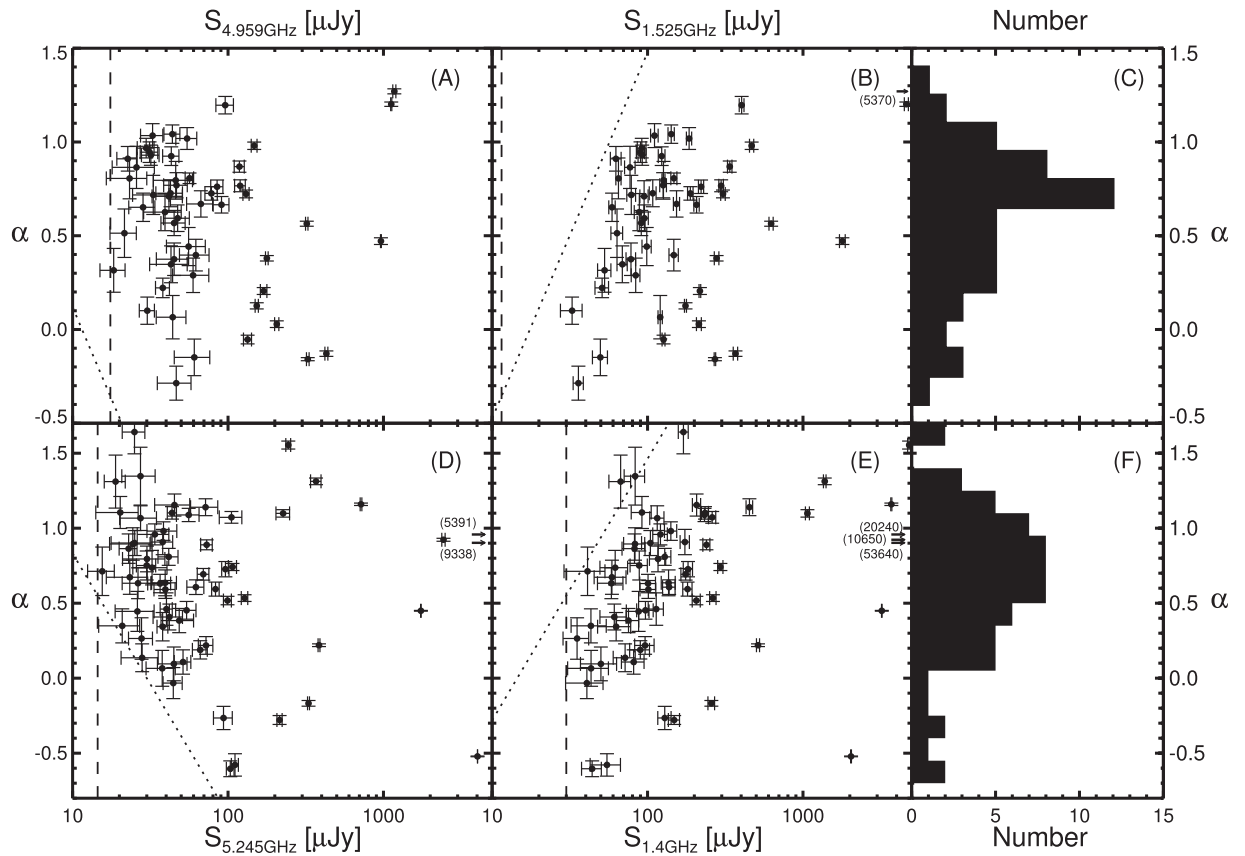


**Figure 4.** Radio spectral index as a function of flux density. The radio spectral indices of our 5 GHz radio sources are plotted as functions of flux densities at 5.0 GHz (panel (A)), 1.5 GHz (panel (B)) for the GN field, and 5.2 GHz (panel (D)) and 1.4 GHz (panel (E)) for the GS field with  $5\sigma$  flux limits of each survey (dashed line; i.e.,  $17.5 \mu\text{Jy}$  (A),  $11.5 \mu\text{Jy}$  (B),  $15 \mu\text{Jy}$  (D), and  $30 \mu\text{Jy}$  (E)). The sources located outside the panels are marked with arrows, and their flux densities are given inside the parentheses. The dotted line in each panel represents the sensitivity of radio spectral index limited by the survey limit of adjacent survey. Histograms of SI distribution for the GN and GS fields are shown in panels (C) and (F), respectively.

SFGs (44%), and quiescent galaxies (31%). The fraction of quiescent galaxies among source undetected in radio is the same as radio detected sources. Therefore, the main difference is in the fraction of SBs. In all cases, the radio detected galaxies trace the high stellar mass envelope for all types of galaxies, independent of  $\Delta_{\text{SFR}}$ , and this is a natural consequence of a flux-limited survey, as demonstrated by our selection function shown in Figure 3. Since our radio observations trace the synchrotron emission from star formation and AGN activities, these statistics imply that our radio survey is not deep enough to detect the star formation activity in the star-forming MS galaxies in the full range of redshift probed, even with  $\mu\text{Jy}$  sensitivity. We discuss this finding in more detail in Section 7.1.

### 5.2. Star Formation Activity and Radio Spectral Index

An apparent correlation between radio spectral index and star formation property ( $\Delta_{\text{SFR}}$ ) is hinted in the color-coded data for radio spectral index in Figure 6. Steep spectrum sources with  $\alpha > 0.5$  (green and blue) appear predominantly in the  $\Delta_{\text{SFR}} > -0.2$  region, while sources with a flat or inverted spectrum ( $\alpha < 0.5$ , yellow and orange) appear mostly in the region below  $\Delta_{\text{SFR}} = -0.2$ . This might be an indication that steep spectrum sources are abundant among SFG+SB galaxies with  $\Delta_{\text{SFR}} > -0.2$ , while few steep spectrum sources are in the quiescent galaxy region with  $\Delta_{\text{SFR}} < -0.2$ .

This apparent trend is examined more directly in Figure 7 by plotting the radio spectral index as a function of  $\Delta_{\text{SFR}}$ . What is apparent now is that the SFG+SB galaxies are more tightly clustered around  $\alpha \sim 0.8$ , while the quiescent galaxies ( $\Delta_{\text{SFR}} < -0.2$ ) are distributed more uniformly, spanning a nearly twice as large range in spectral index  $\alpha$ —the SFG+SB galaxies have a tighter distribution with a higher mean ( $0.72 \pm 0.05$ ) than the quiescent galaxies ( $0.22 \pm 0.11$ ). The histograms in panel (B) of Figure 7 show these trends clearly with different peak positions—the SFG+SB galaxies (blue) have a peak at  $\alpha \approx 0.8$ , but the quiescent galaxies (red) have a peak at  $\alpha \approx 0.13$ . The two-sided Kolmogorov–Smirnov test for the two samples in R indicates that the null hypothesis of their radio spectral index distributions drawn from the same parent population is rejected with a  $p$ -value of 0.0015. This result is consistent with the expectation that star formation yields steep radio spectra with  $\alpha \sim 0.8$  through optically thin synchrotron emission produced by supernova shocks (Condon 1992) while AGN are associated with flat or inverted radio spectra with  $\alpha \ll 0.8$  through synchrotron self-absorption (e.g., de Bruyn 1976).

It is tempting to speculate that there is a weak trend of decreasing  $\alpha$  with decreasing  $\Delta_{\text{SFR}}$  if the handful of sources with  $\alpha \geq 1$  in the upper left corner of Figure 7 are ignored. These ultra-steep spectrum sources are generally jet-dominated AGNs, and one could separate them out morphologically, but that kind of handpicking is not generally possible for a study

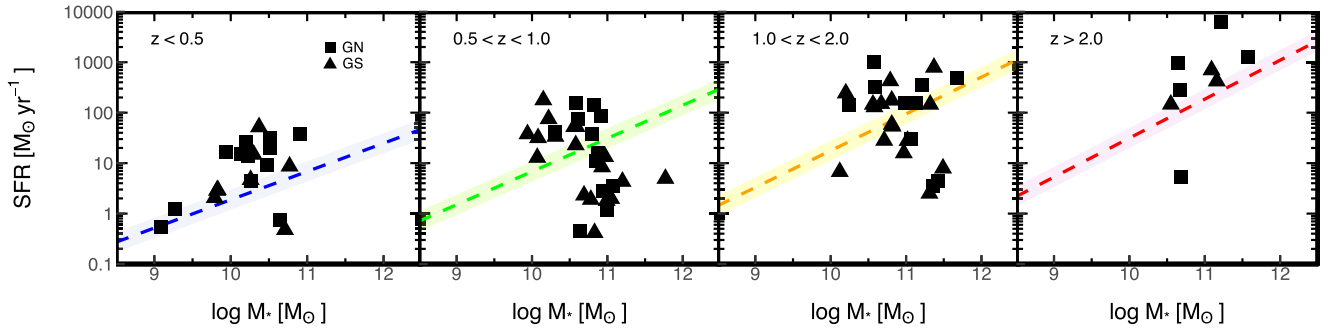


**Figure 5.** SFR and stellar mass distributions of the GS and GN radio sources with respect to the MS in four redshift bins. We represent the SFR and stellar mass distribution of radio sources in GN (squares) and GS (triangles) in four redshift bins,  $z < 0.5$ ,  $0.5 < z < 1.0$ ,  $1.0 < z < 2.0$ , and  $z > 2.0$ . A dashed lines show the SFR–stellar mass relation of the MS at mean redshifts 0.25 (blue), 0.75 (green), 1.5 (orange), and 2.5 (red) with dispersion of  $\pm 0.2$  (shaded regions).

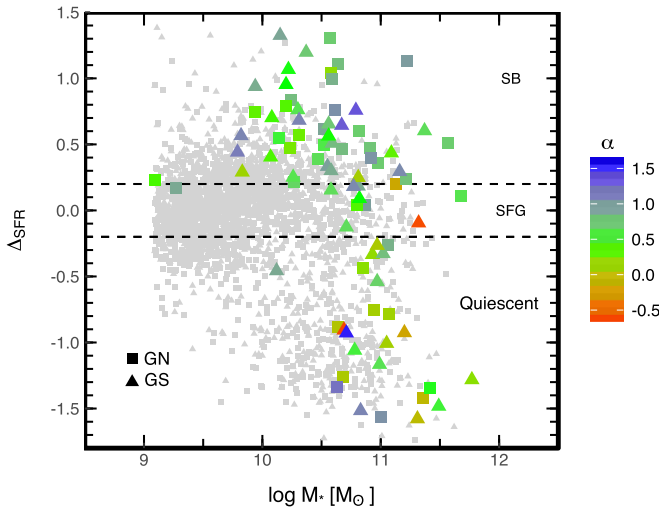


**Figure 6.** Offset of SFR from the MS ( $\Delta_{\text{SFR}}$ ) and stellar mass with a color code according to radio spectral index in GN (squares) and GS (triangles) fields. Small gray points are the 3D-*HST* galaxies without radio counterparts in GN and GS fields for a comparison. The dashed lines of  $\Delta_{\text{SFR}} = \pm 0.2$  indicate the selection of SFGs. SBs are sources above a line of  $\Delta_{\text{SFR}} > 0.2$  while quiescent galaxies are those below a line of  $\Delta_{\text{SFR}} < -0.2$ . The distribution of radio spectral index show that SFG+SB have mainly steep spectra while quiescent galaxies have flatter spectra even though both have wide distributions.

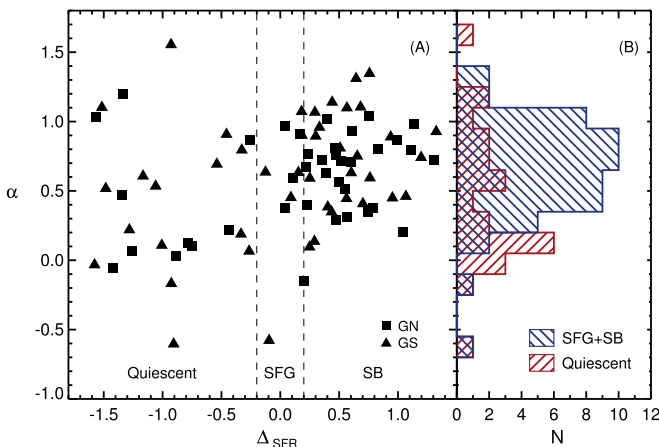


**Figure 7.** Radio spectral index distribution as a function of  $\Delta_{\text{SFR}}$ . Panel (A) shows that the radio spectral index distribution of SFG+SB ( $\Delta_{\text{SFR}} > -0.2$ ) is more tightly clustered around  $\alpha \sim 0.8$ , in comparison with the quiescent galaxies ( $\Delta_{\text{SFR}} < -0.2$ ), which are distributed more uniformly and widely in spectral index  $\alpha$ . These trends are easily seen in the histograms of SFG+SB (blue) and quiescent galaxies (red) in panel (B). The Kolmogorov–Smirnov test indicates that the radio spectral index distributions of the two populations are different from each other with a  $p$ -value of 0.0015.

without the necessary spatial information.<sup>20</sup> The large spread in  $\alpha$  at a given value of  $\Delta_{\text{SFR}}$  also makes such a generalization difficult to trust. What seems to be more certain is that this spread is real and essentially independent of star-forming activity  $\Delta_{\text{SFR}}$ , and this has an important consequence for understanding and modeling the nature of faint radio population and their evolution, as we discuss in more detail later.

## 6. Radio–FIR Correlation of Radio Sources

The radio–FIR correlation is one of the robust indicators of star formation and black hole activities (Helou et al. 1985; Condon 1992; Yun et al. 2001; Bell 2003). In particular, the radio–FIR correlation of SFGs is a tight correlation with a less than 0.3 dex scatter over five orders of magnitudes in luminosity (Yun et al. 2001), and this obviously indicates that a strong coupling exists between dust-reprocessed emission of ultraviolet radiation from massive young stars and synchrotron radiation by cosmic rays accelerated in SNe II (Condon 1992). In this section, we examine the radio–FIR correlation of the  $\mu\text{Jy}$  radio sources identified in the GN and GS fields as a function of their star formation properties and their measured radio spectral index.

The rest-frame radio–FIR correlation parameter,  $q_{\text{FIR}}$  is defined as

$$q_{\text{FIR}} = \log_{10} \left( \frac{L_{\text{FIR}} [\text{W}]}{3.75 \times 10^{12} \text{ Hz}} \right) - \log_{10} P_{1.4 \text{ GHz}} [\text{W Hz}^{-1}], \quad (3)$$

where  $L_{\text{FIR}}$  is a rest-frame FIR luminosity from 40 to 120  $\mu\text{m}$  (Helou et al. 1985; Yun et al. 2001). The radio–FIR correlations of radio sources as a function of redshift are shown in Figure 8 for GN (squares) and GS (triangles), color-coded by  $\Delta_{\text{SFR}}$ . The overwhelming majority of the SFG+SB population (86%) follow the local radio–FIR correlation for SFGs (Yun et al. 2001), and galaxies near the star-forming MS ( $-0.5 \leq \Delta_{\text{SFR}} \leq +0.5$ ) nearly exclusively fall within the gray band shown in the left panel of Figure 8. On the other hand, only  $\sim 30\%$  of the quiescent galaxies have  $q_{\text{FIR}}$  of local SFGs, and their radio continuum emission likely has an origin other than star formation. Most of the quiescent galaxies (76% = 19/25) are not detected in the far-IR, and they are marked with a down arrow in Figure 8.

<sup>20</sup> The identification of AGN among the faint radio source population and their impact on observed properties are presented exclusively in Paper II.

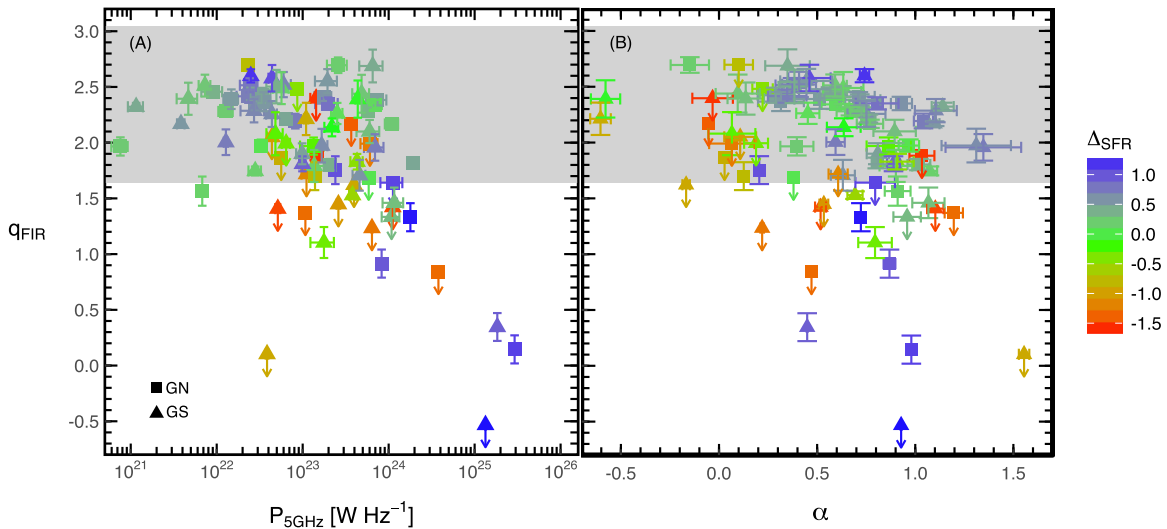


**Figure 8.** Radio–FIR correlation parameter ( $q_{\text{FIR}}$ ) as a function of 5 GHz power (left panel) and radio spectral index (right panel). Radio sources in GN (squares) and GS (triangles) are plotted with the color code of  $\Delta_{\text{SFR}}$  and arrows showing the upper limits. A shaded region represents the range of  $q_{\text{FIR}}$  of local SFGs (i.e.,  $q_{\text{FIR}} = [1.64, 3.04]$ ; Yun et al. 2001). Most SFG+SB (with  $\Delta_{\text{SFR}} > -0.2$ ) are located inside the region of local SFGs while most quiescent galaxies (with  $\Delta_{\text{SFR}} < -0.2$ ) have lower  $q_{\text{FIR}}$ .

A statistical analysis of the radio–FIR correlation for each subpopulation distinguished by its star formation properties shows a clear difference between the SFG+SB galaxies and the quiescent galaxies. We have applied the Kaplan–Meier estimator for  $q_{\text{FIR}}$  of the two subpopulations with the subroutine `cenfit` of the statistical package NADA<sup>21</sup> in R (R Core Team 2017). This analysis shows that the SFG+SB galaxies have a median  $q_{\text{FIR}}$  value of  $2.26 \pm 0.09$ , in good agreement with the local canonical value  $\langle q_{\text{FIR}} \rangle \approx 2.3$  (Yun et al. 2001), while the quiescent galaxies have a median value of  $1.10 \pm 0.10$ . The difference in these median values is quite substantial with a significance of  $\sim 8.8\sigma_c$  (the combined uncertainty for both populations is  $\sigma_c = 0.13$ ). To quantify the difference of radio–FIR correlation distributions between SFG+SB and quiescent galaxies further, we perform the Log-rank test with left-censored data using the `cencliff` function in the NADA in R (R Core Team 2017). This test indicates that the SFG+SB galaxies and the quiescent galaxies have entirely different distributions of  $q_{\text{FIR}}$  with a  $p$ -value of  $< 2 \times 10^{-6}$ . These statistical tests confirm the results of previous studies that the radio–FIR correlation is a powerful tracer of star formation activity (Yun et al. 2001; Bell 2003).

An obvious trend seen in the left panel of Figure 8 is the decreasing  $q_{\text{FIR}}$  with increasing 5 GHz radio power. A straightforward interpretation is that radio AGN contribution is increasing both fractionally and in absolute value for the most radio luminous objects at  $P_{5\text{GHz}} \geq 10^{24} \text{ W Hz}^{-1}$ . A somewhat surprising fact is that the majority of these “radio-excess” objects with  $P_{5\text{GHz}} \geq 10^{24} \text{ W Hz}^{-1}$  are also intensely starbursting galaxies with  $\Delta_{\text{SFR}} \gtrsim 1$ . Similar objects found in the local Universe are mostly Seyfert AGNs associated with a nuclear starburst, but they are exceedingly rare, accounting for only 1% of the *IRAS* 2 Jy Sample studied by Yun et al. (2001). One might conclude a sharp increase (up to  $\sim 5\%$ ) of such AGN+SB hybrid objects at  $z > 1$ , but our sample size is too small to be highly quantitative. Furthermore, survey depth and sample definition might have a strong influence in such an

inference as even our  $\mu\text{Jy}$  sensitivity is not sufficient to probe the MS SFGs (see below Section 7.1). Indeed, both the AGN fraction and the radio-excess fraction reported by the deeper survey of the COSMOS field by Smolčić et al. (2017) are much higher,  $\sim 20\%$ , at the  $S_{1.4\text{GHz}} = 50 \mu\text{Jy}$  and rising up to  $\sim 50\%$  at  $S_{1.4\text{GHz}} = 100 \mu\text{Jy}$  (see their Figure 12). A similar result was also reported by a study with a different AGN identification using the VLBA observations on the same field, where the AGN fraction is  $> 40\%–55\%$  at  $100 < S_{1.4\text{GHz}} < 500 \mu\text{Jy}$  (Herrera Ruiz et al. 2018).

The dependence of radio–FIR correlation on radio spectral index is examined on the right panel of Figure 8, and the quiescent galaxies with  $\Delta_{\text{SFR}} \leq -0.2$  show systematically lower  $q_{\text{FIR}}$  (on average by 0.6–0.8) compared with the SFG+SB population, nearly independent of radio spectral index  $\alpha$ . An in-depth analysis of the similarities and differences among these different subpopulations is discussed in our next paper (Paper II), but this is another indication that quiescent galaxies are indeed a distinct population in their radio and IR properties as well. It is interesting that the extreme steep spectrum quiescent galaxies identified in Figure 7 and discussed in Section 5.2 are *not* extreme outliers and instead nearly follow the normal radio–FIR correlation. A real outlier in the distribution is again the radio-excess SBs with  $\Delta_{\text{SFR}} \gtrsim 1$  discussed previously, and their radio spectral index is typically around  $\alpha \sim +0.9$ , indistinguishable from the bulk of the normal SFGs and SBs. Intense starbursts associated with massive galaxies in the local universe, such as luminous infrared galaxies (LIRGs) and ultraluminous infrared galaxies (ULIRGs), are associated with high free–free opacity, leading to the flattening of radio spectrum (e.g., Klein et al. 2018) and even obscuring a radio AGN altogether at longer wavelengths (e.g., Mrk 231). Therefore, the distribution and geometry of starburst activity in these  $z > 1$  luminous radio-excess SBs are somehow different from local examples. And they certainly cannot be identified from their luminosity and radio spectral index alone. Future higher resolution observations that can resolve the star-forming structures and kinematics are required to yield deeper insight on these sources.

<sup>21</sup> Nondetects and Data Analysis for Environmental Data.

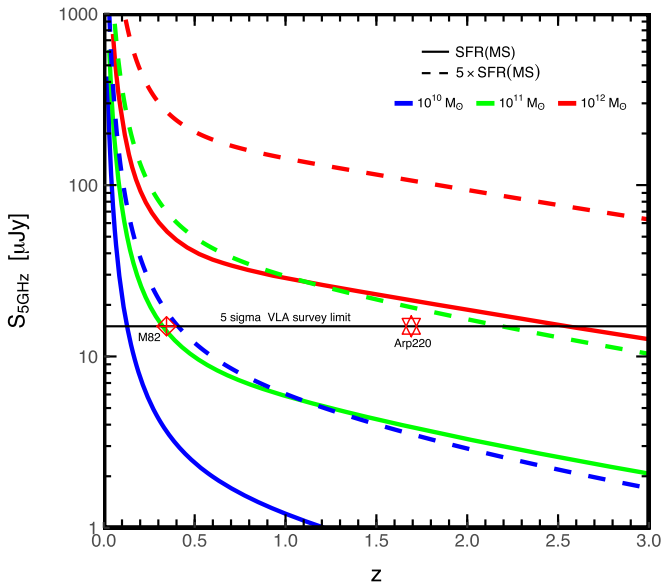


**Figure 9.** Detectability of MS SFGs and a sensitivity of radio observations. We show the observable galaxies with a certain SFR and stellar mass as a function of redshift. We show SFGs with SFR of MS (solid lines) and  $5 \times$  SFR of MS (dashed lines) as a function of redshift with respect to the stellar masses of  $10^{10} M_{\odot}$  (blue),  $10^{11} M_{\odot}$  (green), and  $10^{12} M_{\odot}$  (red). The survey limits ( $5\sigma$ ) of our radio observations are indicated by the horizontal lines (i.e.,  $15 \mu\text{Jy}$  for GS). The evolution of the SFR of MS galaxies is incorporated using the relation derived by Speagle et al. (2014). As examples, we marked the maximum redshifts of detecting M82-like (red diamond) and Arp220-like (red star) galaxies at the survey limits.

## 7. Discussion

### 7.1. Importance of Survey Sensitivity

What makes deep radio continuum imaging attractive as a tool for studying galaxy evolution is the high angular resolution of an interferometer like the VLA to deliver spatial information at much better than  $1''$ , free from the fundamental limits of source confusion that restrict the usefulness of current infrared facilities such as *Herschel*. Advances in sensitivity through increased bandwidth and collecting area also enable us to probe SFGs and AGN population at cosmological distances directly. One of the main goals of this VLA study of the GOODS cosmology fields is to analyze the nature of the faintest radio continuum sources detectable with the current technology and establish technical specifications for future surveys for galaxy evolution using facilities such as MeerKAT, ASKAP, and eventually the Square Kilometer Array.

The plot of rest-frame 5 GHz radio power versus spectroscopic redshift shown in Figure 3 and the analysis of their star formation properties discussed in Section 5 clearly demonstrate that our deep 5 GHz continuum data indeed probes star-forming galaxies out to  $z \sim 3$ . On the other hand, our detailed examination of their specific SFR shown in Figure 6 finds that the fraction of SBs (58%) in our radio sources are more than twice the fraction among the parent general galaxy population in the 3D-*HST* survey. Since there are no reasons for radio-selected SFGs to be fundamentally different from optical or UV selected SFGs, this statistical difference is likely the result of the combined effects of our survey depth and the strong evolution of cosmic SFR density (see review by Madau & Dickinson 2014).

To explore this further, we show the calculated 5 GHz radio flux density of SFGs with SFR of MS (solid lines) and  $5 \times$  SFR (dashed lines) for stellar masses of  $10^{10} M_{\odot}$  (blue),

$10^{11} M_{\odot}$  (green), and  $10^{12} M_{\odot}$  (red) in Figure 9. We assume that SFR scales with 1.4 GHz radio power following the radio-total IR correlation with  $q_{\text{TIR}} = 2.64$  (Murphy et al. 2011) and a single average radio spectral index of  $+0.8$  (but see the discussion on potential bias as follows). In general, angular resolution and source size are important considerations for survey sensitivity. Here, we make a simplifying assumption that most sources detected in a deep survey like this are at high redshifts are unresolved or marginally resolved (Owen & Morrison 2008; Murphy et al. 2017; Owen 2018).<sup>22</sup> At our  $15 \mu\text{Jy}$  ( $5\sigma$ ) survey limit for the GS field (black horizontal line), the maximum observable redshifts for star-forming MS galaxies (dashed lines) are  $z = 0.13$  for  $10^{10} M_{\odot}$  (solid blue),  $z = 0.32$  for  $10^{11} M_{\odot}$  (solid green), and  $z = 2.55$  for  $10^{12} M_{\odot}$  (solid red). SFGs with  $5 \times$  SFR of the MS can be detected out to  $z = 0.41$  for  $10^{10} M_{\odot}$  (dashed blue),  $z = 2.19$  for  $10^{11} M_{\odot}$  (dashed green), and  $z > 3$  for  $10^{12} M_{\odot}$  (dashed red). In terms of well-known local SFGs, we can detect M82-like galaxy out to  $z = 0.34$  and Arp220-like galaxy out to  $z = 1.63$ , respectively. Therefore, even with the  $\mu\text{Jy}$  sensitivity we achieved in these two GOODS fields, we can probe a main-sequence SFG with a stellar mass of  $10^{11} M_{\odot}$  only out to  $z \sim 0.3$ , and our survey is strongly biased to ULIRG-like starbursts and AGN-host galaxies at  $z > 1$ .

This same plot also demonstrates that directly probing the evolution of the star-forming MS galaxies will require a *much* deeper survey. To probe a MS SFG with  $\text{SFR} = 10 M_{\odot} \text{yr}^{-1}$  at the Cosmic Noon ( $z = 2.5$ ) at  $5\sigma$ , a 5 GHz radio survey needs to reach a survey sensitivity of  $28 \text{ nJy}$  with the Next Generation VLA or Square Kilometer Array. This required sensitivity is  $\sim 11.5$  times deeper than the existing deepest 5 GHz continuum survey of the HUDF by Rujopakarn et al. (2016) and *more than 100 times deeper* than our own surveys presented here.

### 7.2. Importance of Angular Resolution

In the previous section, we discussed the importance of sensitivity in probing SFGs at cosmological distances and the requirement for future surveys to improve the sensitivity by more than an order of magnitude to probe the evolution of the main-sequence SFGs. However, another surprising outcomes of our deep VLA 5 GHz surveys is that simply obtaining a deeper data itself does not guarantee probing much deeper into the luminosity function. As discussed in Section 2.1.4, the comparison of the past and recent deep surveys seems to suggest that the rise in source density is *apparently* much flatter than the Euclidean case. Obviously this is not an entirely fair and rigorous comparison, and the situation is quite a bit more complex.

A potentially important experimental parameter here is angular resolution. Both statistical (e.g., Windhorst et al. 1990; Morrison et al. 2010) and direct imaging (e.g., Chapman et al. 2004) studies have shown that faint radio sources have an intrinsic size of  $1''$ – $2''$ . Resolving sources with an angular resolution higher than the intrinsic size can negatively impact deep surveys of SFGs in two ways: (1) by fragmenting

<sup>22</sup> Median of radio source sizes reported at 1.4 GHz by Owen & Morrison (2008) and Owen (2018) are  $1''.2$ – $1''.5$ , while the median source size at 10 GHz reported by Murphy et al. (2017) is  $0''.17 \pm 0''.03$ . The apparent difference in these median radio source sizes is likely attributable to the structures present in these radio sources and the differences in the surface brightness sensitivity achieved.

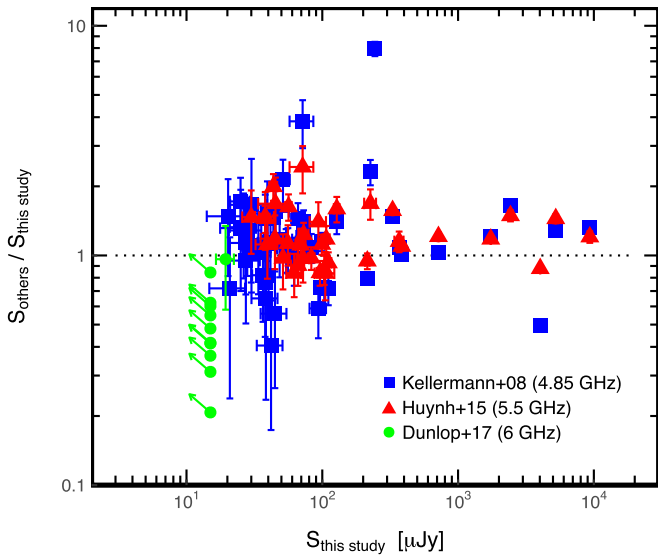


**Figure 10.** Measured flux density comparison among the radio sources in the GS field with those reported by previous studies with different angular resolution. Those by Kellermann et al. (2008) and Huynh et al. (2015) with  $\sim 3$  times larger beams are on average  $\sim 30\%$  larger. The higher resolution survey by Rujopakarn et al. (2016) with  $0''.61 \times 0''.31$  beam has only one detected source in common (the 6 GHz source flux densities are actually reported by Dunlop et al. 2017) that agrees well with ours. The dotted line is the unity ratio line to guide the eye.

individual radio sources into multiple components, especially in the low S/N regime; and (2) loss of surface brightness sensitivity and the resulting loss of extended emission. The former is a well-known phenomenon for nearly all deep radio surveys, and most previous studies have produced catalogs of “source components” as well as integrated source catalogs. In analyzing the  $0''.5$  imaging data of the GN field, Guidetti et al. (2017) identified the loss of surface brightness sensitivity and their bias toward compact sources as the primary cause for their extra-ordinarily high AGN fraction. Only a modest (a factor of  $\sim 3$ ) increase in the source density reported by Rujopakarn et al. (2016) in their ultra-deep imaging of the GS field with nearly 10 times better sensitivity than our survey is likely driven by the loss of flux density and surface brightness sensitivity resulting from their using very high angular resolution ( $0''.61 \times 0''.31$ ).

We explore the impact of angular resolution on flux recovery further by comparing the measured flux density of the faint radio sources in the GS field reported by different surveys with varying angular resolution in Figure 10. The flux densities reported by Kellermann et al. (2008) at 4.85 GHz and by Huynh et al. (2015) at 5.5 GHz were both measured using a  $\theta \approx 4''$  beam, and these flux densities are systematically higher when compared with our measurements obtained with a  $1''.5$  beam. The average flux ratio between the Kellermann et al. (2008) flux density to our flux density is 1.34, with a median ratio of 1.14. Similarly, the average and median ratios of the Huynh et al. (2015) flux density to our flux density is 1.26 and 1.18, respectively. A small correction due to intrinsic spectral index is neglected, as both low angular resolution measurements are significantly larger (about 30%) than our measurements with an effective center frequency of 5.25 GHz. These measured differences are much larger than the expected absolute calibration uncertainties ( $\lesssim 10\%$ ) associated with the standard flux density bootstrapping calibration. The comparison with the higher resolution ( $0''.61 \times 0''.31$ ) imaging

by Rujopakarn et al. (2016) does not provide much new insight, as there is only one source in common.

In summary, observing angular resolution smaller than the expected intrinsic radio source size of  $1''\text{--}2''$  can lead to a significant systematic bias in deep radio surveys. Carefully accounting for this resolution effect and surface brightness sensitivity is an important consideration for all future ultra-deep surveys with nJy sensitivity.

### 7.3. Importance of Accurate Radio Spectral Index

Obtaining accurate radio spectral indices is an important step in studying the radio–FIR correlation and its evolution over the cosmic time because computing the rest-frame radio–FIR correlation requires a correction with a “ $\log_{10}[(1+z)^{1-\alpha}]$ ” dependence on radio spectral index, associated with the  $k$ -correction for the observed radio power. This has the largest impact at the highest redshifts, where the evidence for any evolution in the radio–FIR correlation is expected to be the most pronounced.

Many previous studies of faint radio source population have applied only a partial correction for this spectral index effect, largely because of practical constraints, but the magnitude of the resulting error may have been under-appreciated. Ideally, one should obtain observations at two different frequencies with matched beams and depths to derive correct radio spectral index. However, conducting observations in *two* frequency bands can be prohibitively expensive in telescope time, especially for deep surveys that require tens to hundreds of hours of integration time in each band. Instead, a common practice is to take advantage of existing survey at another frequency, as we have done using the existing 1.4 GHz surveys by Miller et al. (2013) and by Owen (2018). If the complementary archival data are not readily available in raw format as is often the case, however, radio spectral index has to be computed without the beam correction (e.g., Ivison et al. 2010a; Bourne et al. 2011; Magnelli et al. 2015; Delhaize et al. 2017). Alternatively, a number of other studies have resorted to adopting a single average radio spectral index of 0.7 to 0.8 instead (e.g., Appleton et al. 2004; Ibar et al. 2008; Murphy et al. 2009; Ivison et al. 2010b; Sargent et al. 2010; Mao et al. 2011). Because even SFGs at  $z \geq 1$  are resolved at  $\sim 1''$  scales, ignoring this resolution effect can lead to significant systematic errors in computing the total radio power and the radio spectral index. Similarly, the radio spectral index distribution is intrinsically broad as discussed in Section 4, and adopting a single value of  $\alpha$  can introduce significant errors in the derived source properties. Here, we analyze both of these issues quantitatively using our GN and GS deep survey data with and without the appropriate corrections.

#### 7.3.1. Importance of Beam-matching for the Radio Spectral Index Calculation

A measured radio spectral index is a direct indicator of the primary radiation mechanism for the observed radio power. In this section, we compare the radio spectral index estimated without matching beam sizes ( $\alpha_{\text{non}}$ ) and with those with matched beams ( $\alpha_{\text{beam}}$ ), to quantify the importance of the beam effect. The ratio of beam areas is mostly between 1.2 and 1.9 for the GN sources, while the GS sources have an average beam area ratio of 10.2, requiring a much larger correction.

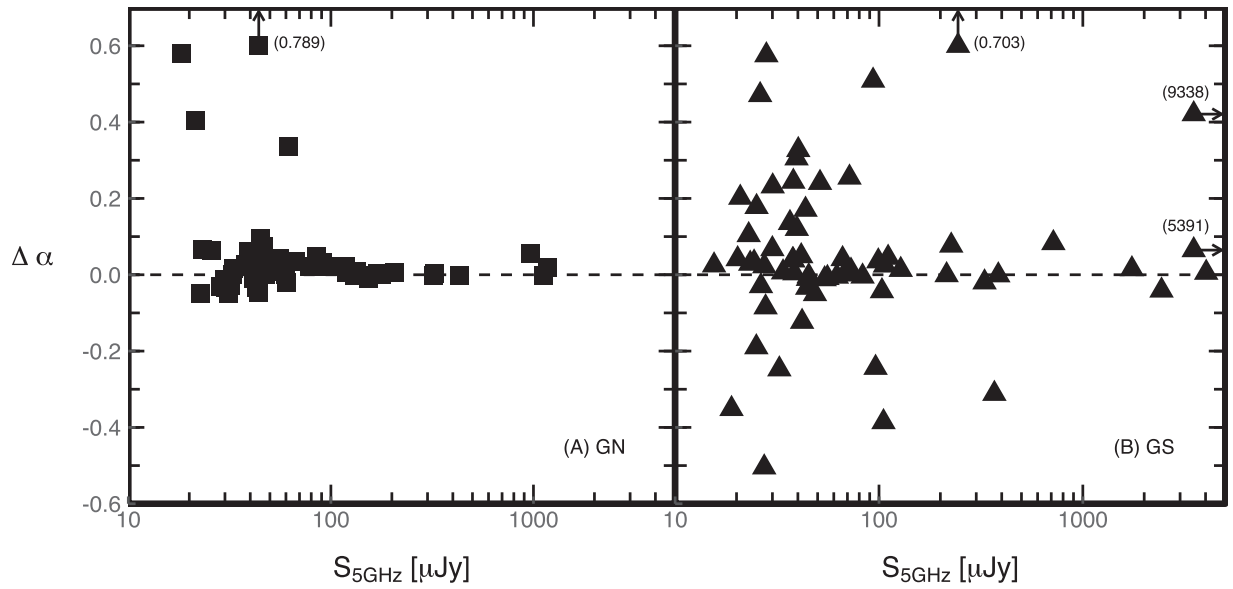


**Figure 11.** Deviations of radio spectral index measured without matching the beam sizes ( $\alpha_{\text{non}}$ ) from that measured by matching beam sizes ( $\alpha_{\text{beam}}$ ). The deviation of radio spectral index ( $\Delta\alpha = \alpha_{\text{non}} - \alpha_{\text{beam}}$ ) is shown as a function of 5 GHz flux density for the GN field (left panel) and for the GS field (right panel). The main difference is the much larger synthesized beam for the 1.4 GHz data in the GS field.

The impact of ignoring the beam size difference is clearly shown in the plot of the deviation of radio spectral index  $\alpha_{\text{non}}$  from  $\alpha_{\text{beam}}$  ( $\Delta\alpha \equiv \alpha_{\text{non}} - \alpha_{\text{beam}}$ ) as a function of total 5 GHz flux density in Figure 11. In the GN field (left panel), where the synthesized beams of 5 and 1.4 GHz data are closely matched, the change is small for most objects as expected. A few sources still show a large deviation with a large positive  $\Delta\alpha$  value, indicating that extended or blended sources can lead to large errors in derived spectral indices, even when the beam size difference is relatively small. Otherwise the observed scatter is consistent with the expected increase in the noise of the 5 GHz data by the larger photometry aperture. The scatter in the derived spectral index is much larger in the GS field (right panel), and this reflects the impact of a much larger beam difference. As in the GN field, the source distribution is biased to the large positive  $\Delta\alpha$  values with a mean of 0.054, especially among  $S_{5\text{GHz}} \geq 1$  mJy sources that are usually associated with extended radio jet sources.

This analysis clearly demonstrates that a small but non-negligible fraction of radio sources are resolved at  $1''$  scale by our 5 GHz beam, and beam-matching is critically important in deriving a correct radio spectral index. This analysis also indicates that our deep 5 GHz data might suffer from loss of flux density due to spatial filtering, even after the beams are matched by smoothing. These combined effects lead to a systematic bias to a steeper (more positive) spectral index and smearing of the overall spectral index distribution, as seen in Figure 4 and discussed in section Section 4. Indeed, all interferometric observations are subject to loss of flux density, and matching the resolution to source size is the best that can be done without obtaining additional data.

### 7.3.2. Impact of Spectral Index on Radio–FIR Correlation

The rest-frame radio–FIR correlation depends on the radio spectral index through the  $k$ -correction for the rest-frame radio power, and there are two common ways which incorrect radio spectral index has impacted the radio–FIR correlation analysis in the literature: (a) not matching beams; and (b) adopting

a single value of  $\alpha$ . Here, we demonstrate how both of these errors in radio spectral index can lead to systematic deviations in the derived radio–FIR correlation parameters  $q_{\text{FIR}}$  using our data. The deviation of radio–FIR correlation is defined as  $\Delta q_{\text{FIR}} \equiv q_{\text{FIR}}(\alpha_{\text{non}}) - q_{\text{FIR}}(\alpha_{\text{beam}})$  (for the unmatched beam case), and they are shown as a function of redshift, color-coded by  $\Delta_{\text{SFR}}$ , in Figure 12.

As discussed in the previous section, the net effect of not correcting for the beam size difference is overestimating radio spectral indices (for this study, because of the higher angular resolution of the 5 GHz data), which in turn leads to a larger  $k$ -correction and an overestimation of the rest-frame radio power. As shown on the left panel of Figure 12, the overall scatter in  $\Delta q_{\text{FIR}}$  resulting from not matching the beams is not large, less than 0.1 in dex. However, all sources with a significant deviation in  $q_{\text{FIR}}$  are *nearly uniformly and systematically toward a lower value with a mean scatter of  $-0.019$ , and this bias is larger in magnitude at a higher redshift* because of a larger  $k$ -correction.

The common practice of adopting a single “average” value (e.g.,  $\alpha = 0.8$ ) leads to an even greater scatter and a stronger bias in  $q_{\text{FIR}}$  than the unmatched beam case, as shown on the right panel of Figure 12. The magnitude of the scatter in  $\Delta q_{\text{FIR}}$  is now nearly 0.2 in dex, approaching the *total* intrinsic scatter in the observed radio–FIR correlation for the local SFGs (Yun et al. 2001). In addition,  $\Delta q_{\text{FIR}}$  is heavily biased toward the negative values with a mean of  $-0.061$  (and growing with redshift), as is the case for the unmatched beam. Both of these trends are the direct results of the large and asymmetric spread in the measured radio spectral index distribution shown in Figure 4.

The fact that both of these common errors in radio spectral index can lead to a significant scatter and a strong bias in the derived  $q_{\text{FIR}}$  is a serious concern for the study of the faint radio source population in general and the study of radio–FIR correlation specifically. The magnitude of the error grows systematically with redshift and is more biased to a lower value of  $q_{\text{FIR}}$ , and this has an important consequence for the evaluation of possible evolution of the radio–FIR correlation.

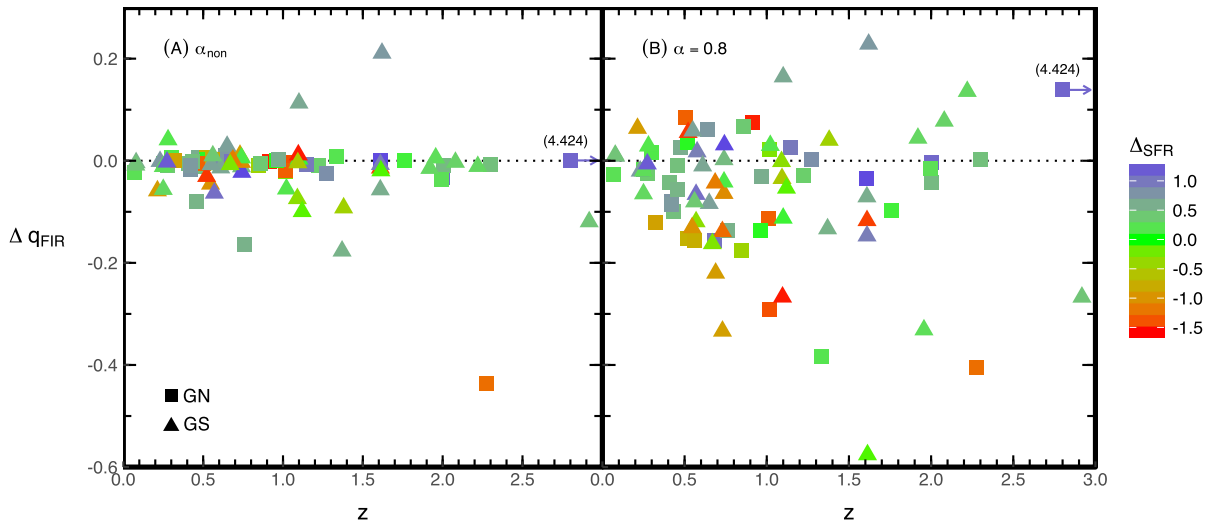


**Figure 12.** Deviations of derived radio–FIR correlations resulting from errors of radio spectral index. The deviation of radio–FIR correlation parameter is shown as a function of redshift, where the deviations of radio–FIR correlations are originated by the radio spectral index by unmatched beam,  $\Delta q_{\text{FIR}} = q_{\text{FIR}}(\alpha_{\text{non}}) - q_{\text{FIR}}(\alpha_{\text{beam}})$ , in the left panel and by adopting a single value of  $\alpha = 0.8$ ,  $\Delta q_{\text{FIR}} = q_{\text{FIR}}(\alpha = 0.8) - q_{\text{FIR}}(\alpha_{\text{beam}})$  in the right panel.

We will discuss this effect in the context of radio–FIR correlation evolution in Paper II.

## 8. Conclusions

We reported the first results from our deep and wide VLA 5 GHz surveys of the GN and GS fields with the resolution and sensitivity of  $\theta = 1''.47 \times 1''.42$  and  $\sigma = 3.5 \mu\text{Jy beam}^{-1}$  and  $\theta = 0''.98 \times 0''.45$  and  $\sigma = 3.0 \mu\text{Jy beam}^{-1}$ , respectively. The central deep cosmology fields with *HST* and other multi-wavelength data are covered with a nearly uniform sensitivity and resolution, and a total of 52 and 88 sources are identified at  $\geq 5\sigma$  significance in the 109 and 190 arcmin<sup>2</sup> survey areas, respectively. We have carefully derived their radio spectral indices by utilizing the existing 1.4 GHz images and catalogs by Owen (2018) and by Miller et al. (2013) and examined the radio spectral index distribution and radio–FIR correlation using only a subset of 84 sources with a reliable spectroscopic redshift to minimize introducing additional scatter. Some of the main results from our analyses of these data include

1. The radio spectral index is measured from beam-matched images of 1.4 and 5 GHz, and its distributions show the clustering of faint radio sources with  $S_{5 \text{ GHz}} \lesssim 150 \mu\text{Jy}$  at around the steep radio spectral index of  $\alpha \sim 0.8$ , which has not seen in previous studies. The associated peak in the GN field is more distinct than in the GS field where the distribution is more smeared out by higher noise. The overall spectral index distribution derived is quite broad, ranging  $-0.5 \leq \alpha \leq 1.4$ , as many earlier studies have reported.
2. The star formation activity is characterized by the distance from the “star formation main sequence” (Speagle et al. 2014), taking into account the strong evolution of SFR with redshift. The majority of faint radio sources are identified as SBs (58%), while only 12% is identified as star-forming MS galaxies with  $|\Delta_{\text{SFR}}| \leq 0.2$ . The remaining 30% are quiescent galaxies with  $\Delta_{\text{SFR}} \leq -0.2$ . This high frequency of SBs is traced to the relatively poor sensitivity of even this deep continuum survey to normal MS SFGs at  $z \geq 0.5$ , and future surveys with up to 100 times better sensitivity

( $\sigma_{5 \text{ GHz}} \lesssim 30 \text{ nJy}$ ) are needed in order to trace the evolution of the star-forming MS at the Cosmic Noon ( $z = 2.5$ ). Our comparison of flux density measurements and source density at different angular resolution support the  $\sim 1''$  extent of intrinsic radio source size reported by previous studies (e.g., Windhorst et al. 1990; Chapman et al. 2004; Morrison et al. 2010), and future ultra-deep surveys should carefully consider the resolution effects (e.g., such as surface brightness sensitivity as well).

3. The SFG+SB population shows a significantly tighter distribution of spectral index than the quiescent galaxies, as shown in Figure 7, suggesting a systematically different origin for their radio emission. The overwhelming majority of the SFG+SB population (86%) follow the local radio–FIR correlation for SFGs (Yun et al. 2001) with a median  $q_{\text{FIR}}$  value of  $2.26 \pm 0.09$ . Only  $\sim 30\%$  of quiescent galaxies follow the same trend, with a median  $q_{\text{FIR}}$  value of  $1.10 \pm 0.10$ —most of the quiescent galaxies (76%) are not detected in any of the *Herschel* far-IR bands. The fraction of radio-excess objects with  $q_{\text{FIR}} \leq 1.6$  increases with increasing 5 GHz radio power, especially for objects at  $z \geq 1$  with  $P_{5 \text{ GHz}} \geq 10^{24} \text{ W Hz}^{-1}$ , and the majority of these objects are intense starburst galaxies with  $\Delta_{\text{SFR}} \gtrsim 1$ . This may indicate a sharp rise in the AGN+SB hybrid population at these redshifts, as suggested by previous studies.
4. Determining and applying correct radio spectral indices is important for deriving accurate radio power and analyzing the radio–FIR correlation. Using our own survey data, we demonstrate that the common practice of not matching the beams carefully can lead to a significant and strongly bias estimation of  $\alpha$  and overestimation of radio power for high redshift sources. More importantly, as shown in Figure 12, the widely used practice of adopting a single “characteristic” value of spectral index ( $\alpha \approx 0.7\text{--}0.8$ ) leads to a much greater scatter matching or exceeding the intrinsic scatter seen in the local population and also a strong systematic bias to negative  $q_{\text{FIR}}$  values, resulting from the broad width and the asymmetry in the intrinsic radio spectral index distribution.

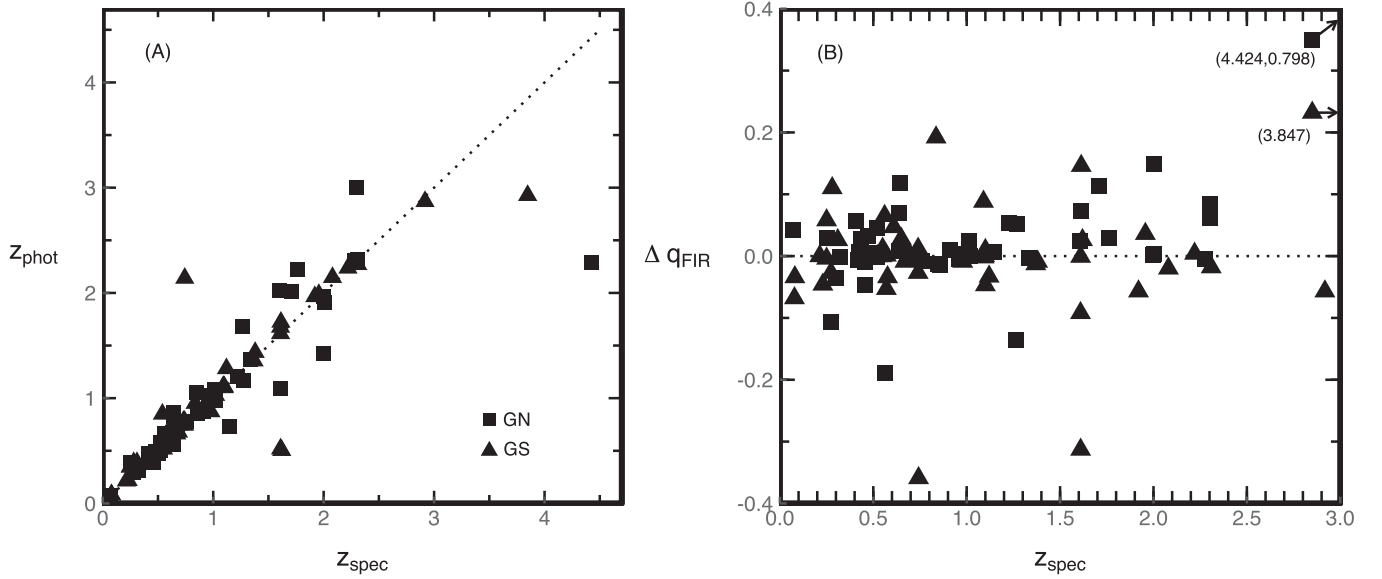


**Figure 13.** Comparison of the photometric and spectroscopic redshifts from the 3D-*HST* project (left panel) and the resulting error in the radio–FIR correlation parameter ( $\Delta q_{\text{FIR}}$ ) as a function of spectroscopic redshift (right panel). The additional scatter in  $\Delta q_{\text{FIR}}$  resulting from using photometric redshift is 0.112 in dex.

Lastly, analyzing our data using the photometric redshifts from the 3D-*HST* project leads to an additional scatter of 0.112 dex in the derived radio–FIR correlation (see Appendix A). The resulting scatter is nearly symmetric, unlike the errors in spectral index discussed previously, and analyzing a much larger sample with high-quality photometric redshifts might be acceptable for future studies requiring much better statistics.

We are grateful to Ryan Cybulski, Stéphane Arnouts, Olivier Ilbert for the use of Le Phare; Katherine E. Whitaker for help in using the 3D-*HST*; and Daniel Q Wang for a discussion of X-ray AGN and HMXBs. We also thank Urvashi Rau for a discussion about the radio imaging and Ken Kellermann for a valuable discussion. H.B.G. extends special thanks to NRAO employees for their hospitality when he was visiting NRAO at Socorro, New Mexico, and for valuable assistance offered through the NRAO help desk. I.A. acknowledges the support via the Conacyt project FDC-2016-1848. We appreciate the anonymous referees for helping us improve this paper.

*Facilities:* Very Large Array, *Herschel Space Observatory*, *Hubble Space Telescope* (3D-*HST*).

*Software:* CASA, AIPS, R, IDL, Python.

### Appendix A

#### Spectroscopic Redshifts versus Photometric Redshifts

As discussed in Section 2.2.5, we limit our analysis only to the subsample of GN and GS radio sources with a spectroscopic redshift because we aim to remove any additional and possibly systematic noise introduced by adopting photometric redshifts, at the expense of reducing the total sample size by up to 16%. As shown in Figure 13, photometric redshifts reported by the 3D-*HST* project, derived using the well-sampled and deep UV-to-NIR photometry available in these fields, are quite good in general, with a few catastrophic outliers. When these redshift errors are propagated into the derivation of  $q_{\text{FIR}}$ , as shown on the right panel, the magnitude of additional scatter introduced by using photometric redshifts is 0.112 in dex. This is about 50% of the intrinsic scatter measured among the local sample of IR-selected SFGs by Yun et al. (2001) and thus is

substantial in magnitude. Fortunately, the redshift error and the resulting changes in  $\Delta q_{\text{FIR}}$  seem random and not systematic, and using photometric redshifts might be acceptable in future studies if the analysis requires a much larger sample size for improved statistics.

### Appendix B

#### Catalog of 5 GHz Flux Densities and Spectral Indices of Our Radio Sources

The final radio source catalog is presented in Table 2. It includes all 52 GN and 88 GS sources cataloged from images with original beam sizes. The 5 GHz flux densities listed in Table 2 are measured with the original beam sizes, but the spectral index is derived with the beam-matched catalogs as shown in Section 2.2.1. Eight GS radio sources with original beam sizes are merged into three sources in the image with the beam size matched to that of 1.4 GHz image (refer to Section 2.2.1). Positions of three merged sources (GS-15, GS-44, and GS-73) are found in the beam-matched catalog, but their 5 GHz flux densities are measured from the image with the original beam size. We also list the eight GS sources below the merged sources as GS-15a, -15b, -15c; GS-44a, -44b, -44c; and GS-73a and -73b. The merged sources are not Gaussian-like shapes in the image with the original beam size, so their flux densities are poorly measured by AIPS tasks SAD or JMFIT, which utilize the 2D Gaussian fitting function. For this reason, the flux densities of three merged sources are measured with the AIPS task TVSTAT, which is appropriate for measuring the flux density of the irregular shaped source. The flux density measured with TVSTAT are larger in general than summation over flux densities of individual sources, because the TVSTAT traces flux densities of regions among individual sources.

Data columns of Table 2 are summarized as follows: (1) Source ID (ID); (2) R.A. (R.A. J2000), a unit of (hour, minute, second); (3) uncertainty of R.A., a unit of second; (4) decl. (decl. J2000), a unit of [ $^{\circ}$  ' '']; (5) uncertainty of decl., a unit of ' '; (6) peak flux density ( $S_{\text{peak}}$ ) and its uncertainty, a unit of  $\mu\text{Jy beam}^{-1}$ ; (7) integrated flux density ( $S_{\text{int}}$ ) and its

**Table 2**  
5 GHz Flux Densities and Spectral Indices of GN and GS Radio Sources

ID	R.A. J2000 (h m s)	eR.A. (s)	Decl. J2000 ( $^{\circ}$ ' ")	eDecl. (")	$S_{\text{peak}}$ ( $\mu\text{Jy beam}^{-1}$ )	$S_{\text{int}}^{\text{a}}$ ( $\mu\text{Jy}$ )	$\alpha^{\text{b}}$
GS-01	3 31 59.619	0.034	-27 47 32.87	0.07	27.8 $\pm$ 4.9	27.8 $\pm$ 4.9	0.265 $\pm$ 0.138
GS-02	3 31 59.843	0.011	-27 45 40.88	0.02	96.2 $\pm$ 5.2	96.2 $\pm$ 5.2	0.727 $\pm$ 0.051
GS-03	3 32 1.547	0.006	-27 46 47.84	0.01	550.4 $\pm$ 4.0	9338.2 $\pm$ 78.7	0.903 $\pm$ 0.001
GS-04	3 32 3.667	0.015	-27 46 3.98	0.03	63.8 $\pm$ 4.1	66.3 $\pm$ 7.3	0.189 $\pm$ 0.061
GS-05	3 32 6.446	0.054	-27 47 28.96	0.08	18.2 $\pm$ 3.5	25.1 $\pm$ 7.4	0.901 $\pm$ 0.083
GS-06	3 32 8.538	0.042	-27 46 48.55	0.06	26.7 $\pm$ 3.2	55.8 $\pm$ 9.3	1.088 $\pm$ 0.044
GS-07	3 32 8.673	0.000	-27 47 34.68	0.00	4030.0 $\pm$ 3.0	4030.0 $\pm$ 3.0	-0.521 $\pm$ 0.002
GS-08	3 32 9.716	0.003	-27 42 48.43	0.01	329.5 $\pm$ 4.8	329.5 $\pm$ 4.8	-0.168 $\pm$ 0.019
GS-09	3 32 10.734	0.060	-27 48 7.49	0.08	19.0 $\pm$ 3.0	41.9 $\pm$ 9.0	0.408 $\pm$ 0.086
GS-10	3 32 10.797	0.008	-27 46 28.11	0.01	92.5 $\pm$ 3.2	99.2 $\pm$ 5.8	0.518 $\pm$ 0.028
GS-11	3 32 10.923	0.001	-27 44 15.26	0.00	1589.5 $\pm$ 4.0	1740.9 $\pm$ 7.0	0.449 $\pm$ 0.003
GS-12	3 32 11.501	0.017	-27 48 15.90	0.04	39.8 $\pm$ 3.1	51.4 $\pm$ 6.3	0.108 $\pm$ 0.081
GS-13	3 32 11.532	0.014	-27 47 13.31	0.02	57.5 $\pm$ 3.1	72.9 $\pm$ 6.3	0.889 $\pm$ 0.033
GS-14	3 32 11.615	0.048	-27 50 27.54	0.09	16.2 $\pm$ 3.2	16.2 $\pm$ 3.2	<0.347
GS-15	3 32 13.104	0.020	-27 43 50.95	0.21	...	368.1 $\pm$ 28.5	1.312 $\pm$ 0.022
15a	3 32 13.047	0.095	-27 43 50.60	0.09	25.6 $\pm$ 3.3	159.2 $\pm$ 23.2	...
15b	3 32 13.115	0.056	-27 43 51.63	0.05	32.5 $\pm$ 3.3	90.6 $\pm$ 12.2	...
15 c	3 32 13.139	0.029	-27 43 50.62	0.04	42.7 $\pm$ 3.4	105.5 $\pm$ 11.1	...
GS-16	3 32 13.247	0.033	-27 42 41.31	0.06	30.0 $\pm$ 4.3	30.0 $\pm$ 4.3	0.751 $\pm$ 0.097
GS-17	3 32 13.490	0.008	-27 49 53.11	0.02	87.3 $\pm$ 3.0	103.4 $\pm$ 5.9	-0.604 $\pm$ 0.052
GS-18	3 32 13.898	0.013	-27 50 0.88	0.02	56.4 $\pm$ 3.1	56.4 $\pm$ 3.1	<-0.483
GS-19	3 32 14.164	0.051	-27 49 10.53	0.08	17.9 $\pm$ 2.9	33.8 $\pm$ 7.8	0.959 $\pm$ 0.070
GS-20	3 32 14.213	0.053	-27 46 34.89	0.08	16.6 $\pm$ 3.0	24.4 $\pm$ 6.7	<0.338
GS-21	3 32 14.992	0.033	-27 42 25.49	0.07	24.8 $\pm$ 4.2	24.8 $\pm$ 4.2	<0.238
GS-22	3 32 15.267	0.053	-27 50 19.76	0.12	15.0 $\pm$ 2.9	32.0 $\pm$ 8.5	<-0.143
GS-23	3 32 15.338	0.043	-27 50 37.72	0.09	16.4 $\pm$ 3.0	20.9 $\pm$ 6.1	0.349 $\pm$ 0.114
GS-24	3 32 17.157	0.019	-27 43 3.70	0.04	40.2 $\pm$ 3.6	40.2 $\pm$ 3.6	0.461 $\pm$ 0.108
GS-25	3 32 17.183	0.032	-27 52 21.10	0.05	32.0 $\pm$ 3.3	54.1 $\pm$ 8.1	0.452 $\pm$ 0.059
GS-26	3 32 18.023	0.002	-27 47 18.77	0.00	375.9 $\pm$ 3.0	384.9 $\pm$ 5.2	0.220 $\pm$ 0.009
GS-27	3 32 18.563	0.044	-27 51 34.82	0.07	18.2 $\pm$ 3.1	22.6 $\pm$ 6.1	<0.048
GS-28	3 32 19.052	0.048	-27 52 14.99	0.09	18.2 $\pm$ 3.1	32.4 $\pm$ 8.0	0.737 $\pm$ 0.115
GS-29	3 32 19.310	0.019	-27 52 19.52	0.04	37.7 $\pm$ 3.2	44.4 $\pm$ 6.2	-0.033 $\pm$ 0.103
GS-30	3 32 19.316	0.003	-27 54 6.58	0.00	352.4 $\pm$ 4.3	2432.7 $\pm$ 60.0	0.923 $\pm$ 0.007
GS-31	3 32 19.514	0.012	-27 52 17.87	0.02	63.0 $\pm$ 3.2	69.3 $\pm$ 6.0	0.693 $\pm$ 0.039
GS-32	3 32 19.817	0.012	-27 41 23.10	0.02	83.1 $\pm$ 4.6	83.1 $\pm$ 4.6	0.594 $\pm$ 0.047
GS-33	3 32 21.285	0.016	-27 44 35.90	0.03	43.6 $\pm$ 2.9	43.6 $\pm$ 2.9	1.102 $\pm$ 0.042
GS-34	3 32 22.159	0.058	-27 49 36.76	0.09	14.5 $\pm$ 2.9	23.3 $\pm$ 6.9	0.673 $\pm$ 0.114
GS-35	3 32 22.281	0.032	-27 48 4.83	0.10	15.5 $\pm$ 3.0	15.5 $\pm$ 3.0	0.713 $\pm$ 0.162
GS-36	3 32 22.514	0.017	-27 48 4.99	0.03	38.0 $\pm$ 3.0	38.0 $\pm$ 3.0	0.343 $\pm$ 0.095
GS-37	3 32 22.597	0.028	-27 44 26.11	0.04	30.3 $\pm$ 2.9	41.5 $\pm$ 6.1	0.809 $\pm$ 0.056
GS-38	3 32 22.723	0.037	-27 41 26.79	0.07	28.5 $\pm$ 4.1	44.8 $\pm$ 9.7	0.095 $\pm$ 0.112
GS-39	3 32 24.262	0.039	-27 41 26.81	0.06	31.9 $\pm$ 4.0	47.9 $\pm$ 9.1	<-0.859
GS-40	3 32 24.670	0.045	-27 53 34.37	0.09	19.5 $\pm$ 3.5	24.4 $\pm$ 7.1	0.895 $\pm$ 0.108
GS-41	3 32 25.174	0.051	-27 54 50.31	0.09	24.1 $\pm$ 4.6	30.1 $\pm$ 9.1	0.795 $\pm$ 0.086
GS-42	3 32 25.180	0.035	-27 42 19.15	0.06	23.1 $\pm$ 3.4	27.3 $\pm$ 6.6	1.347 $\pm$ 0.193
GS-43	3 32 26.769	0.037	-27 41 45.98	0.08	23.9 $\pm$ 3.6	36.9 $\pm$ 8.4	<0.084
GS-44	3 32 26.974	0.001	-27 41 7.16	0.01	...	5390.7 $\pm$ 33.0	0.958 $\pm$ 0.002
44a	3 32 26.953	0.001	-27 41 7.88	0.00	1069.0 $\pm$ 4.0	3613.0 $\pm$ 17.0	...
44b	3 32 27.011	0.001	-27 41 5.44	0.00	1079.0 $\pm$ 4.0	1290.0 $\pm$ 8.0	...
44 c	3 32 27.060	0.044	-27 41 3.69	0.03	77.6 $\pm$ 3.9	463.6 $\pm$ 27.2	...
GS-45	3 32 27.018	0.072	-27 42 18.66	0.14	16.4 $\pm$ 3.2	30.1 $\pm$ 8.6	<-0.020
GS-46	3 32 27.728	0.031	-27 50 41.24	0.05	18.9 $\pm$ 2.9	18.9 $\pm$ 2.9	1.311 $\pm$ 0.177
GS-47	3 32 28.002	0.024	-27 46 39.65	0.04	30.0 $\pm$ 2.9	39.5 $\pm$ 6.1	0.592 $\pm$ 0.060
GS-48	3 32 28.425	0.037	-27 43 44.85	0.08	15.1 $\pm$ 2.9	15.1 $\pm$ 2.9	<0.740
GS-49	3 32 28.513	0.030	-27 46 58.48	0.06	22.9 $\pm$ 3.0	22.9 $\pm$ 3.0	0.864 $\pm$ 0.098
GS-50	3 32 28.742	0.008	-27 46 20.60	0.01	94.7 $\pm$ 2.9	127.8 $\pm$ 6.1	0.534 $\pm$ 0.022
GS-51	3 32 28.826	0.005	-27 43 55.94	0.01	127.5 $\pm$ 2.8	244.2 $\pm$ 8.8	1.554 $\pm$ 0.027
GS-52	3 32 28.886	0.026	-27 41 29.76	0.04	38.6 $\pm$ 3.9	38.6 $\pm$ 3.9	<-0.464
GS-53	3 32 29.876	0.036	-27 44 25.26	0.14	28.2 $\pm$ 2.5	226.1 $\pm$ 22.7	1.099 $\pm$ 0.025
GS-54	3 32 29.986	0.101	-27 44 5.39	0.14	15.6 $\pm$ 2.6	71.7 $\pm$ 14.2	1.140 $\pm$ 0.056
GS-55	3 32 31.489	0.055	-27 46 23.51	0.09	15.4 $\pm$ 2.8	27.4 $\pm$ 7.3	1.067 $\pm$ 0.082
GS-56	3 32 31.546	0.008	-27 50 29.00	0.01	89.8 $\pm$ 2.9	110.9 $\pm$ 5.8	-0.578 $\pm$ 0.075
GS-57	3 32 33.007	0.033	-27 46 6.64	0.07	16.1 $\pm$ 2.9	16.1 $\pm$ 2.9	<0.597

**Table 2**  
(Continued)

ID	R.A. J2000 (h m s)	eR.A. (s)	Decl. J2000 ( $^{\circ}$ ' ")	eDecl. (")	$S_{\text{peak}}$ ( $\mu\text{Jy beam}^{-1}$ )	$S_{\text{int}}^{\text{a}}$ ( $\mu\text{Jy}$ )	$\alpha^{\text{b}}$
GS-58	3 32 33.446	0.057	-27 52 28.55	0.07	19.0 $\pm$ 2.9	38.4 $\pm$ 8.3	0.981 $\pm$ 0.062
GS-59	3 32 36.185	0.053	-27 49 32.17	0.08	15.1 $\pm$ 2.9	20.3 $\pm$ 6.2	1.105 $\pm$ 0.107
GS-60	3 32 37.734	0.030	-27 50 0.71	0.05	28.3 $\pm$ 2.9	38.0 $\pm$ 6.1	0.908 $\pm$ 0.084
GS-61	3 32 37.768	0.027	-27 52 12.63	0.05	29.5 $\pm$ 3.1	36.6 $\pm$ 6.2	0.631 $\pm$ 0.061
GS-62	3 32 37.890	0.069	-27 53 17.86	0.15	17.1 $\pm$ 3.4	30.5 $\pm$ 8.8	<0.277
GS-63	3 32 38.791	0.033	-27 44 49.28	0.05	22.4 $\pm$ 2.9	26.4 $\pm$ 5.5	0.633 $\pm$ 0.103
GS-64	3 32 38.838	0.076	-27 49 56.60	0.07	15.0 $\pm$ 2.8	28.0 $\pm$ 7.5	0.136 $\pm$ 0.093
GS-65	3 32 39.193	0.053	-27 53 57.94	0.10	22.4 $\pm$ 3.8	48.5 $\pm$ 11.5	0.384 $\pm$ 0.081
GS-66	3 32 39.488	0.024	-27 53 1.87	0.04	40.7 $\pm$ 3.4	62.1 $\pm$ 7.8	0.607 $\pm$ 0.049
GS-67	3 32 43.320	0.034	-27 46 47.01	0.06	19.4 $\pm$ 2.9	19.4 $\pm$ 2.9	<0.256
GS-68	3 32 43.542	0.045	-27 54 55.05	0.07	29.1 $\pm$ 5.8	29.1 $\pm$ 5.8	<0.271
GS-69	3 32 44.051	0.062	-27 51 43.90	0.19	20.9 $\pm$ 2.9	105.2 $\pm$ 17.4	1.072 $\pm$ 0.039
GS-70	3 32 44.275	0.009	-27 51 41.31	0.02	85.1 $\pm$ 3.2	106.9 $\pm$ 6.4	0.741 $\pm$ 0.024
GS-71	3 32 45.401	0.036	-27 43 49.36	0.08	17.2 $\pm$ 3.4	17.2 $\pm$ 3.4	<0.502
GS-72	3 32 45.967	0.038	-27 53 16.25	0.08	25.0 $\pm$ 4.2	25.0 $\pm$ 4.2	1.641 $\pm$ 0.146
GS-73	3 32 46.802	0.008	-27 42 14.40	0.14	...	93.5 $\pm$ 13.0	-0.265 $\pm$ 0.078
73a	3 32 46.770	0.039	-27 42 12.50	0.05	34.2 $\pm$ 4.6	42.8 $\pm$ 9.2	...
73b	3 32 46.884	0.045	-27 42 15.56	0.07	29.4 $\pm$ 4.6	38.8 $\pm$ 9.4	...
GS-74	3 32 47.494	0.040	-27 42 43.97	0.10	21.9 $\pm$ 4.3	21.9 $\pm$ 4.3	<0.737
GS-75	3 32 47.902	0.047	-27 42 33.12	0.10	24.1 $\pm$ 4.3	45.2 $\pm$ 11.5	1.155 $\pm$ 0.074
GS-76	3 32 48.185	0.031	-27 52 57.02	0.06	31.7 $\pm$ 4.1	37.7 $\pm$ 8.0	0.066 $\pm$ 0.120
GS-77	3 32 48.566	0.040	-27 49 34.63	0.05	24.8 $\pm$ 3.0	39.4 $\pm$ 7.2	0.636 $\pm$ 0.086
GS-78	3 32 49.440	0.002	-27 42 35.54	0.00	599.6 $\pm$ 4.7	716.9 $\pm$ 9.1	1.159 $\pm$ 0.008
GS-79	3 32 51.838	0.020	-27 44 37.09	0.03	53.7 $\pm$ 3.7	72.2 $\pm$ 7.7	0.218 $\pm$ 0.059
GS-80	3 32 52.077	0.008	-27 44 25.57	0.01	151.8 $\pm$ 3.8	214.6 $\pm$ 8.2	-0.279 $\pm$ 0.030
GS-81	3 32 52.326	0.055	-27 45 42.24	0.07	19.0 $\pm$ 3.4	26.1 $\pm$ 7.3	0.445 $\pm$ 0.133
GS-82	3 32 53.863	0.045	-27 51 36.91	0.10	21.4 $\pm$ 4.1	29.3 $\pm$ 8.6	<-0.035
GS-83	3 32 59.386	0.050	-27 47 58.50	0.08	22.7 $\pm$ 4.4	28.8 $\pm$ 8.8	<0.040
GN-01	12 36 0.117	0.144	62 10 46.92	0.16	29.0 $\pm$ 5.4	46.1 $\pm$ 13.0	0.796 $\pm$ 0.101
GN-02	12 36 1.803	0.111	62 11 26.34	0.12	32.7 $\pm$ 5.4	32.7 $\pm$ 5.4	1.034 $\pm$ 0.064
GN-03	12 36 3.238	0.070	62 11 10.67	0.07	43.9 $\pm$ 5.2	43.9 $\pm$ 5.2	1.042 $\pm$ 0.049
GN-04	12 36 6.607	0.054	62 9 50.91	0.06	63.0 $\pm$ 4.7	90.8 $\pm$ 10.6	0.665 $\pm$ 0.044
GN-05	12 36 8.122	0.018	62 10 35.70	0.02	158.2 $\pm$ 4.5	169.6 $\pm$ 8.2	0.205 $\pm$ 0.018
GN-06	12 36 8.790	0.295	62 11 43.57	0.15	21.6 $\pm$ 4.2	60.7 $\pm$ 15.6	-0.149 $\pm$ 0.098
GN-07	12 36 12.513	0.158	62 11 40.22	0.16	21.4 $\pm$ 4.0	39.3 $\pm$ 10.7	0.626 $\pm$ 0.099
GN-08	12 36 17.096	0.068	62 10 11.35	0.06	38.0 $\pm$ 3.9	38.0 $\pm$ 3.9	0.222 $\pm$ 0.052
GN-09	12 36 19.453	0.078	62 12 52.47	0.09	31.9 $\pm$ 4.1	31.9 $\pm$ 4.1	0.930 $\pm$ 0.054
GN-10	12 36 20.284	0.022	62 8 44.12	0.02	122.9 $\pm$ 4.3	133.7 $\pm$ 7.9	-0.054 $\pm$ 0.023
GN-11	12 36 21.217	0.122	62 11 8.68	0.17	18.2 $\pm$ 3.5	25.8 $\pm$ 7.8	0.865 $\pm$ 0.112
GN-12	12 36 22.536	0.012	62 6 53.70	0.01	325.8 $\pm$ 6.4	325.8 $\pm$ 6.4	-0.158 $\pm$ 0.008
GN-13	12 36 31.266	0.038	62 9 57.66	0.04	56.5 $\pm$ 3.5	56.5 $\pm$ 3.5	0.806 $\pm$ 0.028
GN-14	12 36 32.480	0.063	62 11 5.19	0.07	30.2 $\pm$ 3.4	30.2 $\pm$ 3.4	0.100 $\pm$ 0.073
GN-15	12 36 34.456	0.043	62 12 13.01	0.05	55.8 $\pm$ 3.3	85.0 $\pm$ 7.6	0.761 $\pm$ 0.036
GN-16	12 36 34.505	0.040	62 12 41.00	0.04	59.8 $\pm$ 3.4	78.1 $\pm$ 7.1	0.726 $\pm$ 0.036
GN-17	12 36 35.608	0.115	62 14 23.97	0.14	23.0 $\pm$ 3.9	33.0 $\pm$ 8.7	0.718 $\pm$ 0.104
GN-18	12 36 37.042	0.074	62 8 52.16	0.09	31.3 $\pm$ 4.0	31.3 $\pm$ 4.0	0.946 $\pm$ 0.055
GN-19	12 36 40.742	0.100	62 10 11.33	0.18	21.9 $\pm$ 3.4	44.1 $\pm$ 9.5	0.065 $\pm$ 0.116
GN-20	12 36 41.563	0.077	62 9 48.16	0.08	29.7 $\pm$ 3.7	29.7 $\pm$ 3.7	0.967 $\pm$ 0.052
GN-21	12 36 42.093	0.016	62 13 31.29	0.02	137.8 $\pm$ 3.5	147.3 $\pm$ 6.3	0.980 $\pm$ 0.020
GN-22	12 36 42.187	0.057	62 15 45.22	0.07	46.3 $\pm$ 4.3	54.5 $\pm$ 8.4	1.018 $\pm$ 0.058
GN-23	12 36 44.390	0.003	62 11 33.05	0.00	641.0 $\pm$ 3.4	963.0 $\pm$ 6.3	0.471 $\pm$ 0.018
GN-24	12 36 46.074	0.100	62 14 48.58	0.09	28.3 $\pm$ 3.6	42.6 $\pm$ 8.3	0.726 $\pm$ 0.072
GN-25	12 36 46.331	0.012	62 14 4.58	0.01	177.7 $\pm$ 3.5	177.7 $\pm$ 3.5	0.380 $\pm$ 0.014
GN-26	12 36 46.334	0.082	62 16 29.25	0.08	47.2 $\pm$ 4.3	95.9 $\pm$ 12.4	1.196 $\pm$ 0.046
GN-27	12 36 46.660	0.104	62 8 33.15	0.09	33.2 $\pm$ 4.6	41.7 $\pm$ 9.2	0.710 $\pm$ 0.083
GN-28	12 36 49.663	0.027	62 7 37.97	0.03	130.6 $\pm$ 5.9	130.6 $\pm$ 5.9	0.723 $\pm$ 0.021
GN-29	12 36 50.181	0.190	62 8 44.80	0.22	22.0 $\pm$ 4.4	59.6 $\pm$ 15.6	0.289 $\pm$ 0.092
GN-30	12 36 51.091	0.082	62 10 30.91	0.08	32.3 $\pm$ 3.7	45.0 $\pm$ 8.0	0.568 $\pm$ 0.067
GN-31	12 36 51.721	0.078	62 12 21.36	0.08	22.6 $\pm$ 3.4	22.6 $\pm$ 3.4	0.910 $\pm$ 0.066
GN-32	12 36 52.814	0.088	62 18 7.95	0.10	44.9 $\pm$ 5.6	66.9 $\pm$ 12.7	0.670 $\pm$ 0.070
GN-33	12 36 52.888	0.012	62 14 43.97	0.01	188.1 $\pm$ 3.5	205.8 $\pm$ 6.4	0.028 $\pm$ 0.018
GN-34	12 36 53.372	0.089	62 11 39.33	0.16	19.7 $\pm$ 3.5	23.3 $\pm$ 6.8	0.806 $\pm$ 0.109
GN-35	12 36 55.800	0.111	62 9 17.32	0.11	30.4 $\pm$ 4.6	45.0 $\pm$ 10.4	0.375 $\pm$ 0.087

**Table 2**  
(Continued)

ID	R.A. J2000 (h m s)	eR.A. (s)	Decl. J2000 ( $^{\circ}$ ' ")	eDecl. (")	$S_{\text{peak}}$ ( $\mu\text{Jy beam}^{-1}$ )	$S_{\text{int}}^{\text{a}}$ ( $\mu\text{Jy}$ )	$\alpha^{\text{b}}$
GN-36	12 36 59.317	0.003	62 18 32.46	0.00	1106.0 $\pm$ 6.0	1122.0 $\pm$ 10.0	1.202 $\pm$ 0.012
GN-37	12 36 59.926	0.110	62 14 49.80	0.15	18.4 $\pm$ 3.4	18.4 $\pm$ 3.4	0.316 $\pm$ 0.117
GN-38	12 37 0.260	0.030	62 9 9.76	0.03	114.2 $\pm$ 5.3	119.7 $\pm$ 9.5	0.766 $\pm$ 0.032
GN-39	12 37 1.558	0.090	62 11 46.40	0.12	28.3 $\pm$ 3.6	47.4 $\pm$ 9.0	0.593 $\pm$ 0.071
GN-40	12 37 2.106	0.115	62 17 34.32	0.16	26.7 $\pm$ 4.5	46.4 $\pm$ 11.4	-0.286 $\pm$ 0.091
GN-41	12 37 8.211	0.128	62 16 59.05	0.13	21.6 $\pm$ 4.1	21.6 $\pm$ 4.1	0.514 $\pm$ 0.129
GN-42	12 37 8.287	0.144	62 10 56.17	0.18	23.4 $\pm$ 4.4	43.0 $\pm$ 11.7	0.348 $\pm$ 0.098
GN-43	12 37 11.327	0.106	62 13 30.91	0.07	30.5 $\pm$ 3.5	46.6 $\pm$ 8.1	0.769 $\pm$ 0.067
GN-44	12 37 13.854	0.011	62 18 26.27	0.01	321.0 $\pm$ 5.8	321.0 $\pm$ 5.8	0.564 $\pm$ 0.013
GN-45	12 37 16.375	0.015	62 15 12.32	0.01	153.0 $\pm$ 3.7	153.0 $\pm$ 3.7	0.126 $\pm$ 0.016
GN-46	12 37 16.672	0.027	62 17 33.39	0.03	108.3 $\pm$ 4.8	118.4 $\pm$ 8.8	0.869 $\pm$ 0.030
GN-47	12 37 21.271	0.008	62 11 29.91	0.01	416.1 $\pm$ 5.3	429.3 $\pm$ 9.4	-0.129 $\pm$ 0.015
GN-48	12 37 25.962	0.024	62 11 28.59	0.01	314.8 $\pm$ 5.6	1174.7 $\pm$ 26.8	1.270 $\pm$ 0.014
GN-49	12 37 30.818	0.066	62 12 58.75	0.07	43.1 $\pm$ 5.2	43.1 $\pm$ 5.2	0.924 $\pm$ 0.050
GN-50	12 37 34.503	0.173	62 17 23.45	0.14	32.3 $\pm$ 6.2	55.8 $\pm$ 15.6	0.442 $\pm$ 0.102
GN-51	12 37 36.922	0.092	62 14 29.51	0.13	28.4 $\pm$ 5.4	28.4 $\pm$ 5.4	0.652 $\pm$ 0.076
GN-52	12 37 42.331	0.091	62 15 18.19	0.11	46.6 $\pm$ 6.4	62.1 $\pm$ 13.4	0.397 $\pm$ 0.084

**Notes.**<sup>a</sup> The integrated flux density is the same as the peak flux density for a point source.<sup>b</sup> The spectral index  $\alpha$  is estimated between 1.4 and 5 GHz using 1.4 GHz images (Owen 2018 for the GN and Miller et al. 2013 for the GS fields) and 5 GHz images with same beam sizes as those of 1.4 GHz images.uncertainty, a unit of  $\mu\text{Jy}$ ; and (8) radio spectral index ( $\alpha$ ) and its uncertainty.**ORCID iDs**Hansung B. Gim  <https://orcid.org/0000-0003-1436-7658>Min S. Yun  <https://orcid.org/0000-0001-7095-7543>Frazer N. Owen  <https://orcid.org/0000-0002-9819-3861>Emmanuel Momjian  <https://orcid.org/0000-0003-3168-5922>Mauro Giavalisco  <https://orcid.org/0000-0002-7831-8751>Grant Wilson  <https://orcid.org/0000-0003-2705-9152>James D. Lowenthal  <https://orcid.org/0000-0001-9969-3115>Itziar Aretxaga  <https://orcid.org/0000-0002-6590-3994>Glenn E. Morrison  <https://orcid.org/0000-0003-2310-4497>Ryohei Kawabe  <https://orcid.org/0000-0002-8049-7525>**References**

- Appleton, P. N., Fadda, D. T., Marleau, F. R., et al. 2004, *ApJS*, 154, 147
- Arnouts, S., Cristiani, S., Moscardini, L., et al. 1999, *MNRAS*, 310, 540
- Balestra, I., Mainieri, V., Popesso, P., et al. 2010, *A&A*, 512, A12
- Barger, A. J., Cowie, L. L., Owen, F. N., Hsu, L.-Y., & Wang, W.-H. 2017, *ApJ*, 835, 95
- Barger, A. J., Cowie, L. L., & Wang, W.-H. 2008, *ApJ*, 689, 687
- Bell, E. F. 2003, *ApJ*, 586, 794
- Bonzini, M., Padovani, P., Mainieri, V., et al. 2013, *MNRAS*, 436, 3759
- Bourne, N., Dunne, L., Ivison, R. J., et al. 2011, *MNRAS*, 410, 1155
- Brammer, G. B., van Dokkum, P. G., Franx, M., et al. 2012, *ApJS*, 200, 13
- Bridle, A. H., & Schwab, F. R. 1999, in ASP Conf. Ser. 180, Synthesis Imaging in Radio Astronomy II, ed. G. B. Taylor, C. L. Carilli, & R. A. Perley (San Francisco, CA: ASP), 371
- Bruzual, G., & Charlot, S. 2003, *MNRAS*, 344, 1000
- Burch, S. F. 1979, *MNRAS*, 186, 519
- Caputi, K. I., Lagache, G., Yan, L., et al. 2007, *ApJ*, 660, 97
- Chabrier, G. 2003, *PASP*, 115, 763
- Chapman, S. C., Smail, I., Windhorst, R., Muxlow, T., & Ivison, R. J. 2004, *ApJ*, 611, 732
- Chary, R., & Elbaz, D. 2001, *ApJ*, 556, 562
- Condon, J. J. 1992, *ARA&A*, 30, 575
- Condon, J. J., Cotton, W. D., Fomalont, E. B., et al. 2012, *ApJ*, 758, 14
- Cooper, M. C., Yan, R., Dickinson, M., et al. 2012, *MNRAS*, 425, 2116
- Cowie, L. L., Barger, A. J., Hu, E. M., Capak, P., & Songaila, A. 2004, *AJ*, 127, 3137
- Dale, D. A., & Helou, G. 2002, *ApJ*, 576, 159
- Dale, D. A., Helou, G., Contursi, A., Silbermann, N. A., & Kolhatkar, S. 2001, *ApJ*, 549, 215
- Damen, M., Labbé, I., van Dokkum, P. G., et al. 2011, *ApJ*, 727, 1
- de Bruyn, A. G. 1976, *A&A*, 52, 439
- Delhaize, J., Smolčić, V., Delvecchio, I., et al. 2017, *A&A*, 602, A4
- Downey, J. L., Rieke, G. H., Pérez-González, P. G., Rigby, J. R., & Alonso-Herrero, A. 2007, *ApJ*, 660, 167
- Donnelly, R. H., Partridge, R. B., & Windhorst, R. A. 1987, *ApJ*, 321, 94
- Dunlop, J. S., McLure, R. J., Biggs, A. D., et al. 2017, *MNRAS*, 466, 861
- Elbaz, D., Dickinson, M., Hwang, H. S., et al. 2011, *A&A*, 533, A119
- Fomalont, E. B., Windhorst, R. A., Kristian, J. A., & Kellerman, K. I. 1991, *AJ*, 102, 1258
- Gim, H. B., Hales, C. A., Momjian, E., & Yun, M. S. 2015, AAS Meeting, 225, 143.40
- Guidetti, D., Bondi, M., Prandoni, I., et al. 2017, *MNRAS*, 471, 210
- Helou, G., Soifer, B. T., & Rowan-Robinson, M. 1985, *ApJL*, 298, L7
- Herrera Ruiz, N., Middelberg, E., Deller, A., et al. 2018, *A&A*, 616, A128
- Huynh, M. T., Bell, M. E., Hopkins, A. M., Norris, R. P., & Seymour, N. 2015, *MNRAS*, 454, 952
- Ibar, E., Cirasuolo, M., Ivison, R., et al. 2008, *MNRAS*, 386, 953
- Ibar, E., Ivison, R. J., Best, P. N., et al. 2010, *MNRAS*, 401, L53
- Ibar, E., Ivison, R. J., Biggs, A. D., et al. 2009, *MNRAS*, 397, 281
- Ilbert, O., Arnouts, S., McCracken, H. J., et al. 2006, *A&A*, 457, 841
- Ivison, R. J., Alexander, D. M., Biggs, A. D., et al. 2010a, *MNRAS*, 402, 245
- Ivison, R. J., Magnelli, B., Ibar, E., et al. 2010b, *A&A*, 518, L31
- Kauffmann, G., Heckman, T. M., White, S. D. M., et al. 2003, *MNRAS*, 341, 54
- Kellermann, K. I., Fomalont, E. B., Mainieri, V., et al. 2008, *ApJS*, 179, 71
- Kirkpatrick, A., Pope, A., Alexander, D. M., et al. 2012, *ApJ*, 759, 139
- Klamer, I. J., Ekers, R. D., Bryant, J. J., et al. 2006, *MNRAS*, 371, 852
- Klein, U., Lisenfeld, U., & Verley, S. 2018, *A&A*, 611, A55
- Kriek, M., van Dokkum, P. G., Labbé, I., et al. 2009, *ApJ*, 700, 221
- Kurk, J., Cimatti, A., Daddi, E., et al. 2013, *A&A*, 549, A63
- Lagache, G., Dole, H., & Puget, J.-L. 2003, *MNRAS*, 338, 555
- Le Fèvre, O., Cassata, P., Cucciati, O., et al. 2013, *A&A*, 559, A14
- Le Floch, E., Papovich, C., Dole, H., et al. 2005, *ApJ*, 632, 169

- Luo, B., Brandt, W. N., Xue, Y. Q., et al. 2017, *ApJS*, **228**, 2
- Lutz, D., Poglitsch, A., Altieri, B., et al. 2011, *A&A*, **532**, A90
- Madau, P., & Dickinson, M. 2014, *ARA&A*, **52**, 415
- Magnelli, B., Elbaz, D., Chary, R. R., et al. 2011, *A&A*, **528**, A35
- Magnelli, B., Ivison, R. J., Lutz, D., et al. 2015, *A&A*, **573**, A45
- Magnelli, B., Popesso, P., Berta, S., et al. 2013, *A&A*, **553**, A132
- Mao, M. Y., Huynh, M. T., Norris, R. P., et al. 2011, *ApJ*, **731**, 79
- McMullin, J. P., Waters, B., Schiebel, D., Young, W., & Golap, K. 2007, in ASP Conf. Ser. 376, *Astronomical Data Analysis Software and Systems XVI*, ed. R. A. Shaw, F. Hill, & D. J. Bell (San Francisco, CA: ASP), **127**
- Mignoli, M., Cimatti, A., Zamorani, G., et al. 2005, *A&A*, **437**, 883
- Miller, L., Peacock, J. A., & Mead, A. R. G. 1990, *MNRAS*, **244**, 207
- Miller, N. A., Bonzini, M., Fomalont, E. B., et al. 2013, *ApJS*, **205**, 13
- Momcheva, I. G., Brammer, G. B., van Dokkum, P. G., et al. 2016, *ApJS*, **225**, 27
- Morris, A. M., Kocevski, D. D., Trump, J. R., et al. 2015, *AJ*, **149**, 178
- Morrison, G. E., Owen, F. N., Dickinson, M., Ivison, R. J., & Ibar, E. 2010, *ApJS*, **188**, 178
- Murphy, E. J., Chary, R.-R., Alexander, D. M., et al. 2009, *ApJ*, **698**, 1380
- Murphy, E. J., Condon, J. J., Schinnerer, E., et al. 2011, *ApJ*, **737**, 67
- Murphy, E. J., Momjian, E., Condon, J. J., et al. 2017, *ApJ*, **839**, 35
- Owen, F. N. 2018, *ApJS*, **235**, 34
- Owen, F. N., & Morrison, G. E. 2008, *AJ*, **136**, 1889
- Padovani, P., Mainieri, V., Tozzi, P., et al. 2009, *ApJ*, **694**, 235
- Perley, R. A., Chandler, C. J., Butler, B. J., & Wrobel, J. M. 2011, *ApJL*, **739**, L1
- Polletta, M., Tajer, M., Maraschi, L., et al. 2007, *ApJ*, **663**, 81
- Popesso, P., Dickinson, M., Nonino, M., et al. 2009, *A&A*, **494**, 443
- Prandoni, I., Parma, P., Wieringa, M. H., et al. 2006, *A&A*, **457**, 517
- Randall, K. E., Hopkins, A. M., Norris, R. P., et al. 2012, *MNRAS*, **421**, 1644
- Ravikumar, C. D., Puech, M., Flores, H., et al. 2007, *A&A*, **465**, 1099
- R Core Team 2017, *R: A Language and Environment for Statistical Computing* (Vienna: R Foundation for Statistical Computing)
- Roseboom, I. G., Ivison, R. J., Greve, T. R., et al. 2012, *MNRAS*, **419**, 2758
- Roseboom, I. G., Oliver, S. J., Kunz, M., et al. 2010, *MNRAS*, **409**, 48
- Rudnick, L., & Owen, F. N. 2014, *ApJ*, **785**, 45
- Rujopakarn, W., Dunlop, J. S., Rieke, G. H., et al. 2016, *ApJ*, **833**, 12
- Sargent, M. T., Schinnerer, E., Murphy, E., et al. 2010, *ApJS*, **186**, 341
- Scoville, N., Lee, N., Vanden Bout, P., et al. 2017, *ApJ*, **837**, 150
- Seymour, N., Dwelly, T., Moss, D., et al. 2008, *MNRAS*, **386**, 1695
- Silverman, J. D., Mainieri, V., Salvato, M., et al. 2010, *ApJS*, **191**, 124
- Skelton, R. E., Whitaker, K. E., Momcheva, I. G., et al. 2014, *ApJS*, **214**, 24
- Smolčić, V., Delvecchio, I., Zamorani, G., et al. 2017, *A&A*, **602**, A2
- Speagle, J. S., Steinhardt, C. L., Capak, P. L., & Silverman, J. D. 2014, *ApJS*, **214**, 15
- Straughn, A. N., Pirzkal, N., Meurer, G. R., et al. 2009, *AJ*, **138**, 1022
- Sutherland, W., & Saunders, W. 1992, *MNRAS*, **259**, 413
- Szokoly, G. P., Bergeron, J., Hasinger, G., et al. 2004, *ApJS*, **155**, 271
- Tanabashi, M., Hagiwara, K., Hikasa, K., et al. 2018, *PhRvD*, **98**, 030001
- Tozzi, P., Gilli, R., Mainieri, V., et al. 2006, *A&A*, **451**, 457
- van der Wel, A., Bell, E. F., Häussler, B., et al. 2012, *ApJS*, **203**, 24
- Vanzella, E., Cristiani, S., Dickinson, M., et al. 2008, *A&A*, **478**, 83
- Wang, W.-H., Cowie, L. L., Barger, A. J., Keenan, R. C., & Ting, H.-C. 2010, *ApJS*, **187**, 251
- Whitaker, K. E., Franx, M., Leja, J., et al. 2014, *ApJ*, **795**, 104
- Whitaker, K. E., Pope, A., Cybulski, R., et al. 2017, *ApJ*, **850**, 208
- Windhorst, R., Mathis, D., & Neuschaefer, L. 1990, in ASP Conf. Ser. 10, *Evolution of the Universe of Galaxies*, ed. R. G. Kron (San Francisco, CA: ASP), **389**
- Wirth, G. D., Trump, J. R., Barro, G., et al. 2015, *AJ*, **150**, 153
- Xue, Y. Q., Luo, B., Brandt, W. N., et al. 2016, *ApJS*, **224**, 15
- Yun, M. S., Reddy, N. A., & Condon, J. J. 2001, *ApJ*, **554**, 803
- Zheng, W., Mikles, V. J., Mainieri, V., et al. 2004, *ApJS*, **155**, 73